Use of remote-sensing reflectance to constrain a data assimilating marine biogeochemical model of the Great Barrier Reef.

Emlyn M. Jones[1], Mark E. Baird[1], Mathieu Mongin[1], John Parslow[1], Jenny Skerratt[1], Nugzar Margvelashvili[1], Richard J. Matear[1], Karen Wild-Allen[1], Barbara Robson[2], Farhan Rizwi[1], Peter Oke[1], Edward King[1], Thomas Schroeder[3], Andy Steven[3] and John Taylor[4]

[1] CSIRO Oceans and Atmosphere, Hobart, Australia, 7000

[2] CSIRO Land and Water, Canberra, Australia, 2601

[3] CSIRO Oceans and Atmosphere, Brisbane, Australia, 4102

[4] CSIRO Data61, Canberra, Australia, 2601

Correspondence to: Emlyn M. Jones (emlyn.jones@csiro.au)

Key words: Great Barrier Reef, Data Assimilation, Remote Sensing, observed OC3M, Reflectances, Biogeochemical (BGC) Model, Chlorophyll

Abstract: Skillful marine biogeochemical (BGC) models are required to understand a range of coastal and global phenomena such as changes in nitrogen and carbon cycles. The refinement of BGC models through the assimilation of variables calculated from observed in-water inherent optical properties (IOPs), such as phytoplankton absorption, is problematic. Empirically-derived relationships between IOPs and variables such as Chlorophyll-a concentration (Chl-a), Total Suspended Solids (TSS) and Color Dissolved Organic Matter (CDOM) have been shown to have errors that can exceed 100% of the observed quantity. These errors are greatest in shallow coastal regions, such as the Great Barrier Reef (GBR), due the additional signal from bottom reflectance. Rather than assimilate quantities calculated using error-prone IOP algorithms, this study demonstrates the advantages of assimilating quantities calculated directly from the less error-prone satellite remote-sensing reflectance. The assimilation of a directly-observed quantity, in this case remote-sensing reflectance, is analogous to the assimilation of temperature brightness in Numerical Weather Prediction (NWP), or along-track sea-surface height in hydrodynamic models. To assimilate the observed reflectance, we use an in-water optical model to produce an equivalent simulated remote-sensing reflectance, and calculate the mis-match between the observed and simulated quantities to constrain the BGC model with a Deterministic Ensemble Kalman Filter (DEnKF). Using the assumption that simulated surface Chl-a is equivalent to remotely-sensed OC3M estimate of Chl-a resulted in a forecast error of approximately 75%. Alternatively, assimilation of remote-sensing reflectance resulted in a forecast error of less than 40%. Thus, in the coastal waters of the GBR, assimilating remote-sensing reflectance halved the forecast errors. When the analysis and forecast fields from

the assimilation system are compared with the non-assimilating model, an independent comparison to in-situ observations of Chl-a, TSS, and dissolved inorganic nutrients (NO_3, NH_4 and DIP) show that errors are reduced by up to 90%. In all cases, the assimilation system improves the result compared to the non-assimilating model. This approach allows for the incorporation of vast quantities of remote-sensing observations that have in the past been discarded due to shallow water and/or artefacts introduced by terrestrially-derived TSS and CDOM, or the lack of a calibrated regional IOP algorithm.

1 Introduction:

Aquatic biogeochemical (BGC) models have been used to understand a range of coastal and global phenomena such ocean acidification (Mongin et al., 2016), nutrient pollution (Skerratt et al., 2013) and carbon cycles, and are central to our predictions of global climate (Sarmiento and Gruber, 2006). At the coastal / regional scale, non-linear biogeochemical processes driven by planktonic interactions, as well as non-linear circulation features such as mesoscale eddies, limit the timescale over which biogeochemical properties are deterministically predictable (Baird, 2010). For the purposes of prediction, it is therefore necessary to assimilate observations to correct for model errors and non-linear processes.

The assimilation of remote-sensing data into marine biogeochemical models has been problematic due to differences between the variables represented in models and the variables that are routinely observed (Baird et al., 2016b). *In situ* observations of phytoplankton pigments and macro-nutrients are sparse in space and time due to the prohibitive expense of collecting them. Optical sensors on gliders and floats provide high resolution *in situ* observations that are used to estimate pigment and nutrient concentrations. Nonetheless, these observations in large parts of the ocean remain sparse. The most spatially comprehensive dataset available for BGC assimilation is from ocean color remote sensing.

It is well known that ocean color algorithms, such as observed OC3M (Moderate Resolution Imaging Spectroradiometer, MODIS, three-band Chl-a algorithm) that are optimized for global applications suffer from errors due to a variety of optically-active constituents in coastal and shelf waters (Odermatt et al., 2012). Furthermore, it has also been noted that even globally there is a non-uniform distribution of error, and substantial bias, in the OC3M-derived chlorophyll-a concentration (Chl-a) . Satellite-derived ocean color products such as Chl-a are a function of observed surface reflectances. A substantial effort is invested in empirical studies that convert reflectance to observable quantities such as Chl-a), Total Suspended Solid concentration (TSS), phytoplankton functional types (PFTs), and Colored Dissolved Organic Matter (CDOM) (Odermatt et al., 2012). Each of these empirical relationships have differing error magnitudes stemming not only from a difference in kind, but also representation errors.

Numerical weather prediction (NWP) overcomes errors due to a difference in kind through using the model to simulate directly observed quantities, such as temperature brightness, in preference to deriving other quantities from brightness measurements and using those derived quantities for model data assimilation. Thus NWP commonly assimilates brightness

temperature in preference to temperature itself (Dee et al., 2011). The goal of this study is apply this approach to marine biogeochemical modelling, assimilating remote-sensing reflectance rather than quantities calculated using error-prone IOP algorithms.

5   The Great Barrier Reef (GBR) is located along the northeast coastline of Australia and is characterized by fringing reefs along the continental slope that create a semi-connected inshore lagoon that spans over 3000 km of coastline (Figure 1). The GBR ecosystem, described as one of the seven natural wonders of the world, is under increasing pressure from local and global anthropogenic stressors (De'ath et al., 2012). Decreasing water clarity
10   due to nutrient and sediment pollution is considered a serious threat to the GBR ecosystem (Thompson et al., 2014), with major concerns being the impact of lower benthic light levels on coral and seagrass communities (Collier et al., 2012; Baird et al., 2016a).

The management of human impacts on the GBR relies on accurate estimates of the
15   biogeochemical state of the coastal ocean. Management authorities use, among other measures, a water quality index that combines estimates of concentrations of suspended sediment, chlorophyll, particulate nitrogen and particulate phosphorus, as well as Secchi depth (Schaffelke et al., 2011). Observations of these quantities come from tens of sites around GBR, which are also used in the skill assessment of the model and assimilation
20   system. Nonetheless, with a 3000 km coastline, *in situ* observations are sparse and intermittent. Ultimately, the most accurate, and best-resolved, estimate of the biogeochemical state of GBR will be obtained through the synthesis of all *in situ* and remotely-sensed observations with additional information from model simulations using a data assimilating system. In this paper, we move towards this goal through assimilation of
25   satellite-derived remote-sensing reflectance, while building confidence in the approach through withholding *in situ* observations for independent model assessment.
The paper is structured in the following manner, in Section 2 (Methods) the data for assimilation and skill assessment is presented, along with a description of the model and assimilation methods used. Section 3 contains the results from the control (no assimilation)
30   run of the model, and subsequent data assimilation experiments. In Section 4 we discuss the approach used and implications of the finding more generally. And we conclude with major findings in Section 5.

2 Methods:

35   ### 2.1 GBR observations

The Integrated Marine Observing System (IMOS) has deployed fluorometers on moorings, gliders and at Yongala and North Stradbroke National Reference Stations (NRS). In this paper we use the monthly observations of dissolved inorganic nutrients (NO_3, NH_4 and DIP)
40   at the NRS sites (Lynch et al., 2014), and IMOS glider transects show the cross-shelf profile of water column properties, including temperature, salinity, and chlorophyll. These locations are shown in Figure 1.

The Australian Institute of Marine Science (AIMS) Reef Rescue network (Figure 1, yellow circles) contains 14 sites in inshore regions and GBR lagoon, and sample nutrients and Chl-a extractions 3 times a year (Thompson et al., 2011; Rolfe and Greg, 2015). The moorings were deployed at the Reef Rescue sites from 2009 to 2014 and included a Sea-Bird water quality monitors (WQM) that measure chlorophyll fluorescence and turbidity (NTU). A comparison of the 2011-2014 control run simulation against the Reef Rescue observations, and other observations, is available at: https://research.csiro.au/ereefs/models.

2.2 MODIS observations

The observed remote-sensing reflectance is obtained from using MODIS-Aqua and an atmospheric correction developed for the region. The atmospheric correction applied an Artificial Neural Network (ANN) approach trained by a radiative transfer model to invert the top of atmosphere (TOA) signal measured by MODIS-Aqua. The ANN algorithm was adapted to an approach previously developed for the MEdium Resolution Imaging Spectrometer (MERIS) sensor but on the basis of a different learning algorithm (Schroeder et al., 2007). Algorithm performance is described in detail in Goyens et al. (2013) and King et al. (2014).

SeaDAS-provided Level-2 flags were used to quality control the observed remote-sensing reflectance and to exclude erroneous and out-of-range pixels. We filtered the data for land and severe sun glint affected pixels, cloud contamination including cloud shadows and rejected pixels with observing and solar zenith angles above 52° and 70°, respectively. For the comparison with model output, the observed remote-sensing reflectance at the centre of the 4 km grid cell is obtained through interpolation from the 1 km observations.

2.3 The eReefs modelling system

We used the eReefs coupled hydrodynamic, sediment and biogeochemical modelling system (Schiller et al 2014). The hydrodynamic model is a fully three-dimensional finite-difference baroclinic model based on the three dimensional equations of momentum, continuity and conservation of heat and salt, employing the hydrostatic and Boussinesq assumptions (Herzfeld 2006; Herzfeld and Gillibrand 2015). The sediment transport model adds a multilayer sediment bed to the hydrodynamic model grid and simulates sinking, deposition and resuspension of multiple size-classes of suspended sediment. (Margvelashvili 2008). The complex biogeochemical model simulates optical, nutrient, plankton, benthic organisms (seagrass macroalgae and coral), detritus, chemical and sediment dynamics across the whole GBR region, spanning estuarine systems to oligotrophic offshore reefs (Baird et al., 2016b). The biogeochemical model considers four groups of microalgae (small and large phytoplankton, *Trichodesmium* and microphytobenthos), 2 zooplankton groups, three macrophytes types (seagrass types corresponding to *Zostera* and *Halophila*, macroalgae) and coral communities. Photosynthetic growth is determined by concentrations of dissolved nutrients (nitrogen and phosphate) and photosynthetically active radiation. Microalgae contain two pigments (chl-a and an assessory pigment), and have variable carbon:pigment ratios determined using a

photoadaptation model (described in Baird et al., 2013). Overall, the model contains 23 optically-active constituents (Appendix A).

The model is forced with freshwater inputs at 21 rivers along the GBR and the Fly River in southwest Papua New Guinea. River flows input into the model are obtained from the DERM (Department of Environment and Resource Management) gauging network. Algorithmic relationships are used to account for nutrient and sediment inputs from rivers into the model (statistical relationships between river flow and nutrient concentrations (Furnas 2003, Furnas et al 2011). Nutrient concentrations flowing in from the ocean boundaries were obtained from the CSIRO Atlas of Regional Seas (CARS) 2009 climatology (Ridgway et al., 2002).

2.4 Calculation of remote-sensing reflectance from biogeochemical state

The model contains 23 optically-active constituents (Appendix A). To calculate the remote-sensing reflectance at the surface, we need to consider the light returning from multiple depths, and from the bottom. Rather than using a computationally-expensive radiative transfer model, we approximate surface reflectance based on an optical-depth weighted scheme (Baird et al., 2016b). The ratio of the backscattering coefficient to the sum of backscattering and absorption coefficients for the whole water column at wavelength, λ, is:

$$\mathbf{u}_\lambda = \int_0^z \frac{w_{\lambda,z'} b_{b,\lambda,z'}}{a_{\lambda,z'} + b_{b,\lambda,z'}} dz' \qquad \text{Eq 1}$$

where $w_{\lambda,z'}$ is a weighting representing the component of the remote-sensing reflectance due to the absorption and scattering at depth z', and z is the bottom depth.

The weighting fraction is given by:

$$\mathbf{w}_{\lambda,z} = \frac{1}{z_1 - z_0} \int_{z_0}^{z_1} \exp\left(-2K_{\lambda,z'}\right) dz' \qquad \text{Eq 2}$$

where K_λ is the vertical attenuation coefficient at wavelength λ and the factor of 2 accounts for the path length of both downwelling and upwelling light. The vertical attenuation coefficient is calculated from the sum of the absorption and scattering properties of each of the optically-active constituents, and the zenith angle (for each of these relationships, and more information, see Baird et al., 2016).

The integral of $w_{\lambda,z'}$ to infinite depth is 1. In areas where light reaches the bottom, the integral of $w_{\lambda,z'}$ to the bottom is less than one, and benthic reflectance is important.

The sub-surface remote-sensing reflectance, r_{rs}, is given by:

$$\mathbf{r}_{rs} = g_0 \mathbf{u}_\lambda + g_1 \mathbf{u}_\lambda^2 \qquad \text{Eq 3}$$

where g_0 = 0.0895 and g_1 = 0.1247 are coefficients for the nadir-view in oceanic waters that vary with wavelength and other optical properties (Morel et al., 2012), but can be

approximated as constants (Lee et al., 2002). The constants result in a change of units from the unitless u to a per unit of solid angle, sr^{-1}, quantity, r_{rs}.

The above-surface remote-sensing reflectance is given by (Lee et al., 2002):

$$\mathbf{R}_{rs,\lambda} = \frac{0.52\, r_{rs,\lambda}}{1 - 1.7 r_{rs}} \qquad \text{Eq 4}$$

Thus, the above-surface remote-sensing reflectance is calculated from the inherent optical properties of the optically-active constituents in the biogeochemical model.

2.5 Data Assimilation System

The Data Assimilation (DA) algorithm used in this study is the Deterministic Ensemble Kalman Filter (DEnKF; Sakov and Oke, 2008). The full biogeochemical state variable list contains over 130 2D and 3D variables, and including all of these in the assimilation system is impractical due to memory constraints, but we also acknowledge that for many variables the observations will be uninformative, and therefore not good candidates to include in the assimilation state vector. We therefore limit the variables that are updated within the system to a select subset that are detailed in Section 2.4.2.

2.5.1 Data Assimilation Algorithm

The DEnKF is based on the Kalman filter analysis equation, of which various flavours have had general success in state estimation in other marine BGC data assimilation problems (e.g. Hu et al., 2012, Ciavatta et al., 2016). The derivation of the DEnKF is given in Sakov and Oke (2008) and is a modification to the traditional Kalman filter equation:

$$\mathbf{x^a} = \mathbf{x^f} + \mathbf{K}(\mathbf{Y} - \mathbf{Hx^f}) \qquad \text{Eq 5}$$

Where **x** is the model state, **Y** is the vector of observations, **H** is the observation operator, and the superscripts of a and f denote the analysis and forecast fields respectively. In this study, we only use a subset of the state variables in the DEnKF update, those variables not included in the state vectors denoted in Table 1 are not altered by the state update. The Forecast Innovations (FI) are defined by:

$$FI = (Y - Hx^f) \qquad \text{Eq 6}$$

The Kalman gain matrix, **K**, is given by:

$$K = lP^f H^T \left(HP^f H^T + R\right)^{-1} \qquad \text{Eq 7}$$

Where l is the localization operator, and **R** is observation error covariance matrix. The background error covariance matrix, **P**, is given by:

$$P^f = \frac{1}{m-1}\sum_{i=1}^{m}(X_i^f - x^f)(X_i^f - x^f)^T = \frac{1}{m-1}AA^T \qquad \text{Eq 8}$$

where m is the ensemble size, and i denotes the ith member of the ensemble. Given that we are using a flavor of the ensemble Kalman filter, the background error covariance is approximated by a 36 member dynamic ensemble whereby X_i^f is the ith ensemble member, and **x** is the ensemble mean. To avoid negative values and normalize the state, we log-transform the state before forming the state vector. The background error covariance matrix is never actually computed, rather a series of anomaly fields are constructed and denoted by **A**. We then construct the Kalman gain matrix in the observation subspace as per Sakov and Oke (2008)

$$A = [A_1 \dots A_m] \qquad \text{Eq 9}$$

where the ith anomaly field is given by:

$$A_i = X_i^f - x^f \qquad \text{Eq 10}$$

where x is the the ensemble mean and is updated via Eq 5, each anomaly field is updated by:

$$A^a = A^f - \frac{1}{2}KHA^f \qquad \text{Eq 11}$$

The full analyzed ensemble is then given by:

$$X^a = A^a + [x^a, \dots, x^a] \qquad \text{Eq 12}$$

The assimilation system iterates through time using a five day forecast length. The assimilation system is cycled by calculating the analysis fields at time t, using the forecast from the previous cycle, $\mathbf{X}^f(t)$, and observations $\mathbf{Y}(t)$ at time (t +/- 3 hrs). The numerical mode is initialized using the analysis fields $\mathbf{X}^a(t)$ and the next five day forecast is made. This forecast at t+5 days, $\mathbf{X}^f(t+5)$, is then used in the next assimilation cycle.

The DEnKF requires the ensemble to be perturbed in such a way that is captures the main source of error. These perturbations are introduced in a way that captures our prior understanding of the the dominant errors. In this system we expect that errors will stem from uncertainty in the Initial Conditions (ICs) as per most assimilation system. Additional sources of error can stem from uncertainty associated with BGC process parameters, which has been discussed at length in Parslow et al. (2013), and river boundary conditions (BCs).

In the context of this study, we have introduced perturbations to the ensemble by sampling initial conditions randomly for a four year run of the BGC model:

$$X(t=0)_i \sim Uniform(X(t=0) , X(t=T)) \quad for\ i = 2 \dots m \qquad \text{Eq 13}$$

Where $\mathbf{X}(t=0)_i$ is the initial condition for the model state for the ith member sampled for a uniform distribution with no replacement. Where $\mathbf{X}(t=0)_{i=1}$ is the ensemble mean. Sensitivity

experiments have shown the model is sensitive to perturbation in the quadratic zooplankton mortality rate for large ($m_{Q,ZS}$) and small zooplankton ($m_{Q,ZL}$) with units of d^{-1} (mg N m^{-3})$^{-1}$. These are considered system parameters, and are as such uncertain. To this end we have perturbed the ensemble, by sampling space and time invariant parameters from:

$$m_{q,ZL,i} \sim LN(0.012, 1) \quad for \ i = 2 \dots m \quad \text{Eq 14}$$
$$m_{q,ZS,i} \sim LN(0.007, 1) \quad for \ i = 2 \dots m \quad \text{Eq 15}$$

Where *LN* is a log-normal distribution. The river nutrient and sediment loads were altered by a time invariant scaling factor (θ) to all rivers:

$$\theta_{NO3,i} \sim N(1, 0.3) \quad for \ i = 2 \dots m \qquad \text{Eq 16}$$
$$\theta_{NH4,i} \sim N(1, 0.3) \quad for \ i = 2 \dots m \qquad \text{Eq 17}$$
$$\theta_{DIP,i} \sim N(1, 0.3) \quad for \ i = 2 \dots m \qquad \text{Eq 18}$$
$$\theta_{FineSed,i} \sim N(1, 0.3) \quad for \ i = 2 \dots m \qquad \text{Eq 19}$$

Where *N* is a normal distribution truncated at 0. Each ensemble member has their load (Q_i) scaled according to:

$$Q_i = \theta_i Q_{control} \qquad \text{Eq 20}$$

where $Q_{control}$ is the load entering the control run.

2.5.2 Assimilation system experiments and configuration

In all experiments we have generated a set of super-observations (Cummings et al, 2005; Oke et al., 2008) by combining the observed atmospherically-corrected remote-sensing reflectance (Schroeder et al., 2008) at 443, 488 and 551 nm into a single observation using the OC3M algorithm:

$$OC3M = 10^{(a0 + a1.B + a2.B^2 + a3.B^3 + a4.B^4)} \qquad \text{Eq 21}$$

Where a0, a1, … a4 are a set of empirically determined coefficients (e.g. NOMAD version 2, http://seabass.gsfc.nasa.gov/wiki/article.cgi?article=NOMAD) and B is:

$$B = log_{10}\left(\frac{R_{rs,\lambda1}}{R_{rs,\lambda2}}\right) \qquad \text{Eq 22}$$

$R_{rs,\lambda1}$ and $R_{rs,\lambda2}$ are determined by the absolute magnitude of the remote-sensing reflectance, and $R_{rs,\lambda1}$ is either the band centred on 443 nm or 488 nm and $R_{rs,\lambda2}$ is the band centred on 551 nm. We apply the OC3M algorithm (Eq. 21) to both the observed and simulated remote-sensing reflectances. Thus when we compare the observed and simulated OC3M, we are comparing two fields that contain the same error characteristics.
The use of the observed OC3M super observation field is advantageous for two reason: 1.) given our system is limited by memory, we can use 3 times more spatial locations if we

assimilate the super-observation OC3M, as opposed to working with the individual spectral bands; and 2.) pthe relationship between individual state variables and remote-sensing reflectances is at times non-linear, thus violating the one of the underlying assumptions of the DEnKF. In contrast, the relationship between simulated and observed OC3M is linear. Additionally, there are strong cross-correlations between the bands. For example, the reflectance at 443 nm is strongly correlated with the reflectance at 488 nm. Therefore, the observations of adjacent bands are no longer independent and it is likely that the assumption that the off diagonal elements of the observation error covariance matrix (**R**), needs to be reconsidered. Using one super-observations eliminates the possibility of cross-correlation.

Four experiments were then undertaken to determine the forecast skill of four different assimilation system configurations using a subset of state variables in the assimilation state vector, and corresponding diagonal elements of the observation error covariance matrix (**R**). We only allow the observations to update the variables contained in the assimilation state vector. The analysed assimilation state vector is then inserted into the full model state vector.

In EXP1, we make the assumption that the observed OC3M is equivalent to the simulated surface Chl-a and use this as the input into the observation operator. In EXP2-4 we assume that the simulated OC3M is equivalent to the observed OC3M and it is used as input into the observation operator.

The assimilation system preserves the stoichiometry of the small and large phytoplankton as follows. In the biogeochemical model, each phytoplankton cell (small, large, benthic or *Trichodesmium*) is represented by a quantity of structural material, B, and reserves of nitrogen, R_N, reserves of phosphorus, R_P, reserves of energy, R_I, and an intracellular chlorophyll-a concentration, c_i. Our intention in the assimilation is to change the number of cells, as quantified by B, not the physiological status of the cell, as represented by R_N, R_P, R_I, and c_i. Since the reserves are quantified as the total of these reserves across the entire population, each of the reserves is changed by the same proportion as the biomass. Thus, for example, the nitrogen reserve of an individual cell, R_N / B, is unchanged. Once the analyzed quantity of c_i is determined (e.g. PhyL_Chl-a and PhyS_Chl-a), the quantities of R_N, R_P, R_I and B are updated such that the respective ratios prior to assimilation are preserved.

3 Results:

3.1 Control Run

The modelling system has been designed to represent the spatially-resolved water quality dynamics (phytoplankton, nutrients, turbidity and oxygen) of the GBR World Heritage Area for informed management. A number of indicators have been used to assess the skill of the model, including RMS errors, Pearson's correlation coefficients, Wilmott's skill indicators (Wilmott et al., 1985; https://research.csiro.au/ereefs/models).

The simulated state variable concentrations resemble both the regional climatology for offshore-reef, lagoon-reef and near-shore zones and water quality observations under contrasting seasons/loads and flood events [not shown here, but detailed at

5   https://research.csiro.au/ereefs/models, with optical (Baird et al., 2016b) and carbon chemistry (Mongin et al., 2016) skill assessment published elsewhere]. As mentioned above, the model simulates remote-sensing reflectance. It is therefore possible to incorporate these reflectances into standard, well-recognized remote-sensing products. Figure 2 presents a snapshot of simulated surface Chl-a and the simulated OC3M, as well as

10 remotely-sensed products (regional ANN-observed OC3M and NASA-observed OC3M).

The two panels on the right side of Figure 2 represent the simulated (top) and remotely-sensed (bottom) OC3M estimate of Chl-a. Both combine individual band remote-sensing reflectance into proxies for Chl-a using the OC3M algorithm. OC3M poorly represents

15 surface Chl-a close to the coast where CDOM absorption dominates). By comparing the two panels, we can conclude that the model represents accurately the general distribution of Chl-a throughout the region, with high values along the coast and above each reef systems, and low concentrations offshore. The simulated surface Chl-a inside the coastal band is higher than in the remotely-sensed observation.

The two panels on the left of Figure 2 represent simulated surface Chl-a (top) and OC3M based on the regionally-optimized remote-sensing reflectance (ANN-observed OC3M). Similar to NASA-observed OC3M, but looking inside the coastal band this time, the general gradient of concentrations are similar in both the simulated OC3M (Figure 2, top right) and

25 the remotely-sensing estimate (Figure 2, bottom left), but the model slightly overestimates OC3M.

3.2 Assimilation system configuration experiments

To choose the best configuration for the assimilation of remote-sensing reflectance into a coastal biogeochemical model, four experiments were undertaken using a variety of state variables in the state vector (**X**, Table 1), and by altering the diagonal elements of the observation error covariance matrix (**R**, Eq 7). The forecast innovations (Eq 6) for the four

35 assimilation system configuration experiments described below are shown in Figure 3:

EXP 1 (green lines, Figure 3): The error-prone assumption that total surface Chl-a is equivalent to observed OC3M is made and is used to calculate the forecast innovations, which are then used to update small and large phytoplankton Chl-a. An 80% error in the

40 ANN-observed OC3M   is prescribed on the diagonal elements of **R**.
EXP 2 (red line, Figure 3): Simulated OC3M (calculated from simulated remote-sensing reflectance at several wavelengths, as described by Baird et al., 2016b) is used to calculate the forecast innovations. The state variable and observation errors are the same as EXP1.
EXP 3 (black line, Figure 3): The same configuration as EXP 2, with a reduced observed error

45 imposed on the diagonal of the observation error covariance matrix.

EXP 4 (blue line, Figure 3): Additional variables are included in the assimilation state vector, which now comprises of small and large phytoplankton, ammonia, nitrate and total suspended solids concentrations. The observation error is the same as EXP3.

5   The forecast innovation (Eq 6) statistics from each experiment (Figure 3) provide insight into the assimilation system performance. An optimal assimilation system should result in mean forecast innovations (mismatches between observations and the model) of close to 0, and low mean absolute innovations. The assimilation system where the observation operator assumed that there was a direct relationship between simulated surface Chl-a and ANN-

10   observed OC3M (EXP1, Figure 3 green line), performed very poorly and was discontinued after 9 cycles; the model at times became numerically stiff, requiring the adaptive ODE integrator to take progressively smaller steps. The innovation statistics for EXP1 suggested the model was constantly over-predicting Chl-a with the mean absolute innovation exceeding 0.7 more than 50% of the time. Calculating the forecast innovations with

15   simulated OC3M and ANN-observed OC3M rather than simulated surface Chl-a and observed ANN-observed OC3M improved innovation statistics dramatically (EXP2-EXP4, Figure 3). The configuration used for EXP4 (Figure 3, blue line) gave the best performance. All subsequent results presented in this study use the EXP4 assimilation system configuration, and we only refer to the ANN-observed OC3M.

20   **3.3 Assimilation system forecast errors in preferred system (EXP 4 configuration).**

The assimilation system was run with a 5-day forecast cycle. Using the forecast at *t+5 days* and comparing the temporal mean of the Root Mean Square Difference (RMSD) and Percentage Error against observations provides insight into the value of the assimilation

25   system, when compared with a non-assimilating system. By comparing the forecast fields against observations, we are providing an independent estimate of forecast skill, as these observations at *t+5 days* have not yet been assimilated by the DA system. Additionally, by comparing the forecast against the persisted analysis field from the previous analysis cycle, it can be determined if the dynamic model is adding skill to the forecast.

A comparison of simulated OC3M and observed OC3M for the non-assimilating control run gives a domain wide median error (range) of 0.32 (0.27 – 0.48) mg m^{-3} (Figure 4). This is approximately equivalent to a domain-wide median percentage error (range) of 100% (80% - 130%) (Figure 4). The data assimilation system reduces the forecast errors and percentage

35   errors to a median value (range) of 0.23 (0.20 – 0.30) mg m^{-3} and 55% (43% - 63%) respectively. The analysis errors are again reduced when observations are assimilated, with median and percentage errors (range) of 0.19 (0.14 – 0.23) mg m^{-3} and 39% (37% - 42%) respectively. When the analysis field from the previous assimilation cycle is persisted forward, the errors (and percentage errors) slightly exceed that of the forecast field with

40   values of 0.26 (0.21 – 0.29) mg m^{-3} and 52% (44% - 65%) respectively. However, it is not expected that these error statistics are spatially uniform given the large percentage of area that is dominated by deep oceanic waters. To understand the spatial variability of the forecast error statistics, the whole domain is divided into three regions representing shallow coastal waters (depth < 30 m), lagoon and shelf waters (30 m < depth < 500 m), and deep

45   oceanic waters (depth > 500 m).

In shallow coastal areas, the non-assimilating control run has a median error (range) of 1.35 (1.1 – 2.45) mg m^{-3}, which corresponds to a percentage error (range) of 130 (105 – 180) %. The distribution of control run errors in the coastal zone is positively skewed, with the mean value of the distribution sitting some way from the median. The assimilation system marginally reduces the median forecast error when compared with the control run, though most notably, it reduces the median percentage error and associated variability. The forecast also beats persistence in this region. There is a marked improvement for lagoon and shelf waters with the assimilation system reducing the median error from 0.34 to 0.25 mg m^{-3}, which corresponds to a reduction in percentage error from 96% to 48%. In the oceanic regions of the domain, the assimilation system reduces the error from 0.16 to 0.10 mg m^{-3}, corresponding to a percentage error reduction from 91% to 45%. In all cases the forecast fields beat persistence. A summary of the results can be found in Table 2 and Table 3.

3.3.1 Forecast, Increment and Analysis Fields

The sum of the surface *Trichodesmium* Chl-a, Small Phytoplankton (PhyS) Chl-a and Large Phytoplankton (PhyL) Chl-a biomass differs substantially from the simulated OC3M as shown in Figure 5. The assimilation system updates all of the state variables included in the assimilation state vector. Simulated OC3M is a diagnostic variable that is a function of all the optically-active dynamic state variables as described in Section 2. To demonstrate the impact on the dynamic variables of PhyS and PhyL, results from the forecast step, and the assimilation update, are presented in Figure 5, Figure 6 and Figure 7.

The simulated OC3M forecast field for cycle 22 (12th September 2013) displays elevated OC3M in the shallow near shore environment throughout the whole of GBR region and southern shelf of Papua New Guinea (PNG) (Figure 5). Additional features are elevated OC3M in the vicinity of the central and southern fringing reefs, and a plume originating from the eastern region of PNG. Offshore oceanic waters generally have low OC3M of 0.2 mg m^{-3} or less. There is some evidence of mesoscale blooms in the northern and southern sections of the domain. Observed OC3M is overlaid on Figure 5 (left). Where there is a difference in colour, the simulated OC3M differs from the observed OC3M.

The forecast surface layer fields for PhyS and PhyL appear substantially different to the simulated OC3M field (Figure 5). There are substantial differences near the coast where TSS and CDOM are known to cause artefacts in OC3M. While there are patchy blooms of small phytoplankton at various locations within the domain, rarely does the PhyS Chl-a exceed 0.5 mg m^{-3}. The exception to this in the inner central coastal region of the GBR and in the vicinity of the Fly River plume on the south coast of PNG. Similarly, the PhyL Chl-a remains very low for large areas of the domain, however in regions with additional nutrient supply (e.g. in upwelling regions, mesoscale eddies and some river mouths) blooms do occur.

When the observed OC3M is assimilated, increment fields are calculated using Equation 5 and are presented in Figure 6 for simulated OC3M, PhyS Chl-a and PhyL Chl-a. The innovations are overlaid on the increment field for OC3M to give an indication of how well we are fitting the observations. In areas where the model is over predicting OC3M, the

increments will be negative. In areas where the model is under predicting the OC3M, the increments will be positive. The increments and innovations here are presented as a fractional change with respect to the background (forecast) field.

5   For this particular analysis cycle, it appears that the model is underestimating inshore OC3M by up to 10-30% and over estimating OC3M by upwards of 50% offshore (Figure 6, left). By using the background ensemble correlation structure, the increments applied to PhyS biomass are to increase its concentration in the inner lagoon by up to 20%, but substantially increase the PhyS biomass offshore of the central outer reefs by more than 50% (Figure 6,
10   centre). It should be noted that the increments being applied to the background fields contain meso and sub-meso scale information. Significantly, features such as upwelling filaments, eddies and plumes are maintained through the assimilation procedure, demonstrating that they are allowed to dynamically evolve in the assimilation system. The increments applied to PhyL biomass (Figure 6, right). differ substantially to those of PhyS
15   biomass (Figure 6, centre). For large areas of the domain, the assimilation system decreases the PhyL biomass by up to 50%, whereas there are some areas that it increases. These areas correspond to regions where a bloom may be occurring. The increment applied to the central region of the domain, offshore of the outer reefs, is linear and coherent and likely a result of shifting a dynamic feature such as an upwelling-induced bloom to better match
20   observations.

When the increments contained in Figure 6 are applied to the forecast fields, the resulting analysis field for simulated OC3M better fits the observed OC3M, with a substantially reduced error inshore and in the vicinity of the outer reefs (Figure 7). The difference
25   between simulated and observed OC3M is small in the deeper offshore regions and shallow sections of the lagoon. The greatest error in OC3M occurs in the central lagoon and the outer reefs where spatial variability is highest. The corresponding analysis fields for small phytoplankton and large phytoplankton are contained in Figure 6. There are elevated concentrations of small phytoplankton biomass in the near shore region near river mouths
30   and the outer fringing reefs. The large phytoplankton biomass is concentrated in the region of Broad Sound, the Fly River plume, and the Papua New Guinea upwelling. Each of these features was predicted by the forecast, as little biomass is added or subtracted by the assimilation update. However, there is substantial removal of large phytoplankton biomass from the northern and central offshore regions. This leaves very little large phytoplankton
35   biomass present in substantial areas of the domain during this particular analysis cycle.

3.3.2 Independent assimilation system assessment: Glider

The control and assimilating runs were compared with an ocean glider that was deployed on 26 May 2013, and recovered on the fourth of August 2013. The glider track largely followed
40   the shelf break and headed in a south-easterly direction. To make a comparison between glider observations and the model, we take a sub sample of glider observations centred at the time of model output, with a time window of two hours. For each glider observation that falls within this time period, we find a corresponding 3-D cell from the model and extract the equivalent model solution. No 3-D interpolation is performed as the non-
45   interpolated solution will yield insight into the unresolved sub grid scale variability. The

unresolved sub grid scale variability is then accounted for in the representation error of the data assimilation system.

A persistent feature seeing in the observed record (Figure 8) is the relatively low Chl-a in the upper 100 m of water column. For much of the record, there is a persistent deep chlorophyll max (DCM) that is centred at between 80 and 120 m depth. Rarely do concentrations in the upper 80 m exceed 0.5 mg/m³. When the control run is examined, Chl-a in the top 80 m regularly exceeds 1 mg/m³, DCMs when they exist, are located between 30 and 60 m deep. A detailed analysis of the control run demonstrates the model is able to reliably produced DCMs, however, in this particular location in time and space, the model does not generate one consistent with the observations. The assimilation system improves the control when compared to the glider, however it cannot place the DCM in the correct location because the remote sensing observations provide no information about such a deep feature. The remote sensing observations do remove the bias in the upper 80 m with concentrations in the assimilating running ranging between 0.1 - 0.3 mg/m³.

A comparison between individual profiles from the glider and equivalent sampling of the model shows substantial unresolved variability. Figure 9A shows that at about 70 m the observed Chl-a as measured by the fluorometer ranges between 0.14 and 0.25 mg/m³, with a mean value of 0.18 mg/m³. These glider profiles fall within two adjacent model cells. The control run gave indistinguishable solutions in these two cells, whereas the assimilating run was different by 0.3 mg/m³ between these two cells. The range in unresolved variability is therefore approximately 50% of the mean value. Similar patterns are seen across most profiles, a sub sample of which are given in Figures 9b-f. The magnitude of the unresolved variability ranges from 5 to 40%. In all cases the assimilation of observed OC3M has reduced the error in the simulated Chl-a when assessed against independent glider data.

The RMSD when calculating for each layer of the model, and aggregated in time for all glider observations, is shown in Figure 10. Above 80 m, there is a substantial reduction in RMSD between the control and assimilating runs. The assimilating run has an RMSD of between 0.10 and 0.17 mg m^{-3} compared with 0.30 to 0.41 mg m^{-3} in the control run. Below 80 m, the RMSD profile is very similar between the control and assimilating run. The observed OC3M constrains the upper 80 m, and does not degrade the solution below 80 m.

3.3.3 Independent assimilation system assessment: In-situ bottle samples

The AIMS Reef Rescue (RR) moorings were deployed at 14 sites in the shallow inshore regions of the Great Barrier Reef Lagoon (Figure 1). The control run typically had RMSDs of between 0.4 and 0.6 mg/m³ of *in situ* Chl-a (Figure 11), with the exception being Geoffrey Bay, which is known to be problematic due to the poor spatial resolution in this area. In most cases the assimilating run reduced the RMSD of *in situ* Chl-a by 10 to 0%.

The TSS RMSD varies widely across all the RR sites (Figure 11), driven by the strong variation in magnitude of the spring – neap tidal forcing. The combination of perturbed forcing, and the inclusion of the TSS constituents in the state vector in the assimilating model, has generated realistic time varying correlations between the observed OC3M and inshore TSS. These cross-correlations allow for the correction of simulated TSS from OC3M observations.

The TSS RMSD at all sites for the assimilating run is less than 5 to 20% that of the control run.

Within the GBR region, there are two IMOS NRS sites (Yongala and North Stradbroke, NS, Figure 1). The dissolved inorganic nutrients of NO_3, NH_4 and DIP are taken monthly. At Yongala, water samples are taken at the surface (0 m), 10 m, 20 m and bottom (26 m). At NS, samples are taken at the surface (0 m), 10 m, 20 m, 30 m, 40 m and 50 m. It should be noted that there are only 3 to 4 samples per depth at each site during the simulation period.. At Yongala, typical RMSDs for NO_3 range from 5 to 12 mg/m³. The improvement at NS is confined to shallow layers above 20 m. Below 20 m the assimilation system degrades the solution by 5 to 15%.

With the exception of the surface samples at Yongala, the assimilation system improved the prediction of NH_4 at all depths for each site. Most notably was the 70 to 90% reduction in RMSD at the deeper locations at Yongala. There were marginal improvements to DIP, which displayed a 0 to 30% reduction in RMSD across all sites.

4 Discussion

In the optically-complex waters of the GBR, the use of observed remote-sensing reflectance to constrain the BGC model substantially reduces the errors in OC3M and *in situ* Chl-a, TSS and nutrients. This has been achieved by explicitly assimilating like-for-like variables. The data assimilation is constrained by the mis-match between simulated and observed OC3M. Our approach of simulating the observation is the opposite to the conversion of observed remote-sensing reflectances into modelled variables, e.g. the assimilation of phytoplankton functional types, TSS, CDOM and Chl-a. The conversion of reflectances into derived variables (e.g. Chl-a, PFTs) have associated errors that are as large as 200% is some locations, and can be biased by up to 70%. These errors at times are difficult to characterise in the data assimilation systems, and the analysis fields contain errors that are larger than the forecast or free run model fields. Our system avoids these errors.

One of the most significant sources of errors in algorithms such as OC3M is that they produce a single value for each horizontal pixel, generally considered to be representative of the first optical depth of the water column. If this is to be compared to a single value in biogeochemical model, then it must be assumed that the water column is well-mixed to the optical depth, and that there is an equal optical depth of each of the wavebands used in the algorithm. Both of these conditions are rarely met in coastal waters. Matching remote-sensing reflectance requires no assumptions about the structure of the water column, or of the vertical distribution of the optically-active constituents, because both observed and modelled quantities are two dimensional fields.

In order to visualise the impact of the assimilation system on the prediction of water clarity, we compare the observed true colour (Figure 13) with the simulated true colour of the control run (Figure 14, top left) and the assimilated run (Figure 14, top right). Simulated true colour images are generated from the remote-sensing reflectance at the red, green and blue wavelengths calculated using the optical model and the three dimensional fields of model-predicted 23 optically-active constituents.

The observed true colour image on the 12 Sep 2013 shows brown / yellow features associated with high suspended sediment concentrations. As these concentrations become more diluted, and mixed with phytoplankton, the water appears more greenish blue.

5 Offshore reefs, with clear water above white substrates, appear as light blue features, with the intensity depending on the reef depth. Qualitatively, the control run (Figure 14, top left) does a reasonably good job of reproducing the observed true colour. The quantification of this mismatch can also be done on individual color bands (Baird et al., 2016b). Qualitatively, the control run does not have enough suspended solids in the surface water in the mouth of

10 Broad Sound (22.2°S, 149.5°E), and has too high phytoplankton concentrations offshore, especially in a feature centred at 23°S, 151.5°E. The assimilated run, while not that different to the control run, corrects some of these errors.

To approximately quantify impacts of the assimilation of water clarity, it is possible consider

15 the colour of the added (and subtracted) constituents in the assimilation procedure. To avoid confusion with the phrases 'falsely-coloured' or 'negative', which have distinct meanings in visualisation science, but to still provide a phrase for true colour error, we use the term "off-colour", and distinguish between off-colour that requires correction through addition (Figure 14, bottom left) and subtraction (Figure 14, bottom right). The assimilation

20 procedure added yellow colours (suspended sediment) within Broad Sound and green colours (phytoplankton) in the mouth. Offshore the assimilation removed green, particularly, as noted above at 23°S, 151.5°E. By removing green it made the water more blue (Figure 14, top right).

25 The general methodology presented in this study is similar to that used in numerical weather prediction (NWP). The approach taken here is to avoid the use of an empirical/statistical inverse model, and use a physics-based forward model to predict remote-sensing reflectance centred at the MODIS bandwidths. We then post-process these simulated remote-sensing reflectances into a simulated OC3M. The simulated OC3M is

30 directly comparable to the observed OC3M with both containing sources of error derived from bottom reflectance, and turbid coastal waters. We have taken the final step of converting the simulated remote sensing reflectances into simulated OC3M as it removes a number of non-linarites associated with working on raw reflectances, and the associated correlated observation errors. Additionally, it reduces the size of observation vector by a

35 factor of three, allowing for a greater number of spatial points to be assimilated. By avoiding the use of an inverse empirical statistical model, we are presenting a BGC DA approach that had been adopted by the NWP community decades ago (Dee et al., 2015).
By avoiding the use of IOP / AOP based empirical/statistical products, this approach can take advantage non-ocean-color specific missions such as Himawari 8. The spectral resolution

40 can be altered to simulate reflectances at the Himawari 8 true colour bands. If the Himawari 8 data can be assimilated it will provide a step change in the data available for areas such as the GBR, due to the high spatial resolution (nominally 500 m) and temporal resolution (every 30 minutes). This data density far exceeds that available from orbiting satellites, and will provide coverage similar to the products being assimilated in NWP systems.

45

The underlying configuration of the data assimilation presented in this study requires the dominant error sub-space to be spanned by the ensemble. Pragmatic choices have been

made to allow the system to run on the available compute resources. To this end we have perturbed 2 sensitive model parameters, and river loads of nutrients and sediments. The distributions that have been sampled to perturb the zooplankton mortality rates and θ_i along with their respective shape parameters could be considered a subjective choice.

5   There is substantial scope here to recast the problem with a Bayesian Hierarchical Modelling (BHM) framework (as in Parslow et al., 2013; and Dowd et al., 2014), whereby the prior distribution are assigned to uncertain parameters, and a thorough meta-analysis of the literature could be used to construct informative distributions. The observations could then be used to construct not only a posterior over the state, but a full joint posterior over the

10   state and parameters. Furthermore, we have not allowed uncertainty in the physics to propagate into the BGC solution. We recognise this is a shortcoming of the study, however, given the computational constraints, we are not in a position to expand the ensemble to include physics perturbations (which would require an ensemble that is up to an order of magnitude larger). As more computing power becomes available, ensemble sizes could be

15   increased, stochastic parameterisations introduced (Garnier et al., 2016), and DA methods with less parametric assumptions (e.g. Parslow et al., 2013), could be adopted.

There has been two recent discussion papers released that detail the pathway towards operationalising BGC forecasting systems (Gehlen et al., 2015; and Ford et al., 2016),

20   analogous to the current NWP and hydrodynamic predictions system that routinely run at numerous operational centres. It has been acknowledged that satellite remote sensing will play a key role in such systems, there appears to be two divergent pathways to achieve this vision. Ford et al., (2016) advocate for the assimilation of empirical statistical products such as Chl-a, diffuse attenuation coefficients and Phytoplankton Functional Types (PFTs), with

25   the alternative being the assimilation of AOPs such remote-sensing reflectances (or subsequent functional derivatives). For complex coastal regions that are dominated by case 2 waters, the assimilation of remote-sensing reflectances avoids the costly requirement of calibrating a empirical/statistical algorithm that is regionally-specific. We advocate a third approach – the assimilation of remote-sensed reflectance.

30   **5 Conclusion**

In this study we have used a spectrally-resolved optical model coupled to a BGC model to simulate the remote-sensing reflectances centred at the MODIS ocean colour bands. The non-linear observation operator in the assimilation system subsequently converted remote-sensing reflectance into a simulated OC3M approximation of Chl-a. Observed OC3M is then

35   assimilated into the model, which reduces the domain-wide forecast errors in Chl-a from 100% to 55% when compared to the non-assimilating model. By using a functional derivation of the remote-sensing reflectances (OC3M), we halve the forecast error compared to simply assuming the OC3M is directly related to the model prediction of surface total Chl-a. A comparison against in-situ observations of NO_3, NH_4, DIP and TSS

40   shows the assimilating model reduces the MAPE from 90% to less than 20% at most stations. By using a forward model that includes a majority of error sources present in the observed OC3M, we have shown that the assimilation of remotely-sensed products in optically complex case 2 waters can be achieved, and adds substantial predictive skill when compared to the non-assimilating model. Furthermore, this approach can be generalized to

non ocean–colour specific missions liberating a vast quantity of data that cannot be used using traditional BGC assimilation systems.

Acknowledgements

The model simulations were developed as part of the eReefs project, a public-private collaboration between Australia's leading operational and scientific research agencies, government, and corporate Australia (research.csiro.au/ereefs). Atmospherically-corrected MODIS products were sourced from NASA and the Integrated Marine Observing System (IMOS) - IMOS is supported by the Australian Government through the National Collaborative Research Infrastructure Strategy (NCRIS) and the Super Science Initiative. Simulations and the processing of the remote sensing data was undertaken with the assistance of resources from the National Computational Infrastructure (NCI), which is supported by the Australian Government via NCRIS. We thank the many colleagues involved in developing the eReefs model, particularly Mike Herzfeld, John Andrewartha, Philip Gillibrand, Cedric Robillot and Richard Brinkman. Mark Baird was additionally funded by the CSIRO Wealth from Oceans Flagship, the Gas Industry Social & Environmental Research Alliance (GISERA), CSS FSP and the CSIRO Coastal Carbon Cluster. River flow data and information used to specify river nutrient and sediment loads were provided by the Government of Queensland.

References

Ariathurai, R. & Krone, R. B. 1976. Finite element model for cohesive sediment transport. Journal of the Hydraulics Division, ASCE, 104, HY2, 323–328.

Baird, M. E. (2010) Limits to prediction in a size-resolved pelagic ecosystem model. J. Plankton Res. 32, 1131-1146.

Baird, M. E., M. P. Adams, R. C. Babcock, K. Oubelkheir, M. Mongin, K. A. Wild-Allen, J. Skerratt, B. J. Robson, K. Petrou, P. J. Ralph, K. R. O'Brien, A. B. Carter, J. C. Jarvis, M. A. Rasheed (2016a) A biophysical representation of seagrass growth for application in a complex shallow-water biogeochemical model Ecol. Mod. 325: 13-27.

Baird, M. E., N. Cherukuru, E. Jones, N. Margvelashvili, M. Mongin, K. Oubelkheir, P. J. Ralph, F. Rizwi, B. J. Robson, T. Schroeder, J. Skerratt, A. D. L. Steven and K. A. Wild-Allen (2016b) Remote-sensing reflectance and true colour produced by a coupled hydrodynamic, optical, sediment, biogeochemical model of the Great Barrier Reef, Australia: comparison with satellite data. Env. Model. Software 78: 79-96.

Baird, M. E., P. J. Ralph, K. Wild-Allen, F. Rizwi and A. D. L. Steven (2013). A dynamic model of the cellular carbon to chlorophyll ratio applied to a batch culture and a continental shelf ecosystem. Limnol. Oceanogr. 58, 1215-1226.

Ciavatta, S., Kay, S., Saux-Picart, S., Butenschön, M. and Allen, J.I., 2016. Decadal reanalysis of biogeochemical indicators and fluxes in the North West European shelf-sea ecosystem. *Journal of Geophysical Research: Oceans*. 121, 1824-1845

Collier, C.J.,Waycott, M., McKenzie, L.J., 2012. Light thresholds derived from seagrass loss in the coastal zone of the northern Great Barrier Reef, Australia. Ecol. Indic. 23, 211-219.

Cummings, J.A., 2005. Operational multivariate ocean data assimilation. *Quarterly Journal of the Royal Meteorological Society*, *131*(613), pp.3583-3604.

De'ath, G. K. E. Fabricius, H. Sweatman and M. Puotinen (2012) The 27-year decline of coral cover on the Great Barrier Reef and its causes. PNAS 109, 17995-17999.

Dee, D. P. et al. (2011) The ERA-Interim reanalysis: configuration and performance of the data assimilation system. Q. J. R. Meteorol. Soc. 137: 553 – 597.

Dowd, M., Jones, E. and Parslow, J., 2014. A statistical overview and perspectives on data assimilation for marine biogeochemical models. *Environmetrics*, *25*(4), pp.203-213.

Egbert, G.D. and Erofeeva, S.Y., 2002. Efficient inverse modeling of barotropic ocean tides. Journal of Atmospheric and Oceanic Technology, 19(2), pp.183-204.

Furnas, M. 2003. Catchments and corals: terrestrial runoff to the Great Barrier Reef. Australian Institute of Marine Science, Queensland., 334 p.

Garnier, F., Brankart, J.M., Brasseur, P. and Cosme, E., 2016. Stochastic parameterizations of biogeochemical uncertainties in a 1/4° NEMO/PISCES model for probabilistic comparisons with ocean color data. *Journal of Marine Systems*, *155*, pp.59-72.

Gaspari, G. and Cohn, S.E., 1999. Construction of correlation functions in two and three dimensions. *Quarterly Journal of the Royal Meteorological Society*, *125*(554), pp.723-757.

Gehlen, M., Barciela, R., Bertino, L., Brasseur, P., Butenschön, M., Chai, F., Crise, A., Drillet, Y., Ford, D., Lavoie, D. and Lehodey, P., 2015. Building the capacity for forecasting marine biogeochemistry and ecosystems: recent advances and future developments. *Journal of Operational Oceanography,8*(sup1), pp.s168-s187.

Gillibrand, P.A. and Herzfeld, M., 2016. A mass-conserving advection scheme for offline simulation of scalar transport in coastal ocean models.*Ocean Modelling*, *101*, pp.1-16.

5   Goyens, C., Jamet, C., Schroeder, T., 2013. Evaluation of four atmospheric correction algorithms for MODIS-Aqua images over contrasted coastal waters. Rem. Sens. Env. 131, 63-75.

Gregg, W.W., 2008. Assimilation of SeaWiFS ocean chlorophyll data into a three-
10   dimensional global ocean model. *Journal of Marine Systems*, *69*(3), pp.205-225.

Herzfeld, M. 2006, An alternative coordinate system for solving finite difference ocean models., Ocean Modelling, 14, 174-196.

15   Hu, J., Fennel, K., Mattern, J.P. and Wilkin, J., 2012. Data assimilation with a local Ensemble Kalman Filter applied to a three-dimensional biological model of the Middle Atlantic Bight. *Journal of Marine Systems*, *94*, pp.145-156.

King, E. A., Schroeder, T., Brando, V. E., Suber, K., 2014. A pre-operational System for
20   Satellite Monitoring of the Great Barrier Reef Marine Water Quality. Tech. rep., CSIRO Report, pp56.

Lynch TP, Morello EB, Evans K, Richardson AJ, Rochester W, et al. (2014) IMOS National Reference Stations: A Continental-Wide Physical, Chemical and Biological Coastal Observing
25   System. PLoS ONE 9(12): e113652. doi: 10.1371/journal.pone.0113652.

Madsen, O.S., 1994. Spectral wave-current bottom boundary layer flows, in Coastal Engineering 1994 Proceedings, 24th International Conference Coastal Engineering Research Council/ASCE, pp. 384-398.

Margvelashvili, N., Saint-Cast, F., Condie, S., 2008. Numerical modelling of the suspended sediment transport in Torres Strait. Continental Shelf Research 28, 2241-2256.

Mattern, J.P., Fennel, K. and Dowd, M., 2014. Periodic time-dependent parameters
35   improving forecasting abilities of biological ocean models.*Geophysical Research Letters*, *41*(19), pp.6848-6854

Mongin, M., M. E. Baird, B. Tilbrook, R. J. Matear, A. Lenton, M. Herzfeld, K. A. Wild-Allen, J. Skerratt, N. Margvelashvili, B. J. Robson, C. M. Duarte, M. S. M. Gustafsson, P. J. Ralph, A. D.

L. Steven (2016). The exposure of the Great Barrier Reef to ocean acidification. Nature Communications 7, 10732.

Morello EB, Plagányi ÉE, Babcock RC, Sweatman H, Hillary R, Punt AE (2014) Model to manage and reduce crown-of-thorns starfish outbreaks. Mar. Ecol. Prog. Ser. 512:167-183

Oke, P.R., Brassington, G.B., Griffin, D.A. and Schiller, A., 2008. The Bluelink ocean data assimilation system (BODAS). Ocean Modelling, 21(1), pp.46-70.

Odermatt, D., Gitelson, A., Brando, V.E. and Schaepman, M., 2012. Review of constituent retrieval in optically deep and complex waters from satellite imagery. Remote sensing of environment, 118, pp.116-126.

Oke, P.R. and Sakov, P., 2008. Representation error of oceanic observations for data assimilation. *Journal of Atmospheric and Oceanic Technology*, *25*(6), pp.1004-1017.

Parslow, J. S., Cressie, N., Campbell, E., Jones. E. M., and Murray, L. 2013. Bayesian learning and predictability in a stochastic nonlinear dynamical model. Ecological Applications 23:4, 679-698

Ridgway K.R., J.R. Dunn, and J.L. Wilkin 2002 Ocean interpolation by four-dimensional least squares -Application to the waters around Australia. J. Atmos. Ocean. Tech., 19, 1357-1375.

Robson, B.J., Baird, M. and Wild-Allen, K., 2013. A physiological model for the marine cyanobacteria, *Trichodesmium*. In MODSIM2013, 20th International Congress on Modelling and Simulation. Modelling and Simulation Society of Australia and New Zealand, ISBN (pp. 978-0).

Rolfe, J. and Gregg, D., 2015. Factors affecting adoption of improved management practices in the pastoral industry in Great Barrier Reef catchments. Journal of environmental management, 157, pp.182-193.

Sakov, P. and Oke, P.R., 2008. A deterministic formulation of the ensemble Kalman filter: an alternative to ensemble square root filters. *Tellus A*, *60*(2), pp.361-371.

Schaffelke B, Carleton J, Doyle J, Furnas M, Gunn K, Skuza M, Wright M, Zagorskis I (2011) Reef Rescue Marine Monitoring Program. Final Report of AIMS Activities 2010/11- Inshore Water Quality Monitoring. Report for the Great Barrier Reef Marine Park Authority. Australian Institute of Marine Science, Townsville. (83 p.)

Sarmiento, J. L and N. Gruber (2006) Ocean Biogeochemical Dynamics. Princeton University Press. ISBN: 9780691017075. 528 pp.

Schiller, A., Herzfeld, M., Brinkman, R., Stuart, G., Jan. 2014. Monitoring, predicting and managing one of the seven natural wonders of the world. Bull. Am. Meteor. Soc. 23-30.

Schroeder, T., Behnert, I., Schaale, M., Fischer, J., Doerer, R., 2007. Atmospheric correction algorithm for MERIS above Case-2 water. J. Int. Remote Sens. 28, 1469-1486.

Skerratt, J., Wild-Allen, K., Rizwi, F., Whitehead, J. and Coughanowr, C., 2013. Use of a high resolution 3D fully coupled hydrodynamic, sediment and biogeochemical model to understand estuarine nutrient dynamics under various water quality scenarios. Ocean & coastal management, 83, pp.52-66.

Thompson, A., Costello, P., Davidson, J., Logan, M., Schaffelke, B., Uthicke, S. and Takahashi, M., 2011. Reef rescue marine monitoring program. Report of AIMS Activities–Inshore coral reef monitoring, p.128.

Thompson, A., Schroeder, T., Brando, V.E., Schaffelke, B., 2014. Coral community responses to declining water quality: Whitsunday Islands, Great Barrier Reef, Australia. Coral Reefs 33, 923-938.

Willmott, C.J., Ackleson SG, Davis RE, Feddema JJ, Klink KM,Legates DR, ODonnell J, Rowe CM. 1985. Statistics for the evaluation of model performance. Journal of Geophysical Research 90: 8995-9005.

Appendix A: Detailed description of the eReefs modelling system

The eReefs modelling system is a suite of coupled hydrodynamic, sediment, optical and biogeochemical models specifically tailored to the Great Barrier Reef. The hydrodynamic model is a three-dimensional, finite-difference, baroclinic model based on the three-dimensional equations of momentum, continuity and conservation of heat and salt, employing the hydrostatic and Boussinesq assumptions (Herzfeld et al., 2006, Schiller et al., 2015). The equations of motion are discretized on a finite-difference stencil corresponding to the Arakawa C grid. In the vertical z-coordinate scheme, there are 47 fixed z-levels. The atmospheric forcing products (wind, pressure, rain and heat fluxes) are supplied by Bureau of Meteorology (BOM) reanalysis products. A tidal signal was superimposed on the low-frequency sea level oscillation provided by BRAN2.3 (Oke et al., 2008) on the regional grid open boundary. This tidal signal was introduced via a local flux adjustment. The OTIS tidal model (Egbert and Erofeeva, 2002) was used to generate the tidal signal from amplitude and phase information for 8 constituents. The local grid open boundary was forced with temperature, salinity and velocity (with local flux adjustment) derived from the regional

grid. A mass conserving flux-based advection scheme is used to transport sediment and biogeochemical tracers.

The sediment transport model adds a multilayer sediment bed to the hydrodynamic model grid and simulates sinking, deposition and resuspension of multiply size-classes of suspended sediment (Margvelashvili et al., 2008). The model solves advection-diffusion equations of the mass conservation of suspended and bottom sediments and is particularly suitable for representing fine sediment dynamics, including resuspension and transport of biogeochemical particles. The model is initialised with the observed distribution of gravel, sand and mud in the seabed of the shelf region. Sediment particles settle on the seabed due to gravity and resuspend into the water column whenever the bottom shear stress, exerted by waves and currents, exceeds the critical shear stress of erosion. The resuspension and deposition fluxes are parameterised with the Ariathurai and Krone (1976) formula. The bottom friction under combined waves and currents is estimated through the nonlinear bottom boundary layer model (Madsen, 1994).

Sediments in benthic layers undergo vertical mixing due to bioturbation, represented by local diffusion. The corresponding diffusion coefficient scales with the sediment depth so that the bioturbation ceases to operate beneath the biologically active layer. The resistance of sediments to resuspension also varies with the sediment depth to reflect the consolidated nature of deep sediments. The numerical grid for sediment variables in the water column coincides with the numerical grid for the hydrodynamic model. Within the bottom sediments, the model utilises a time-varying sediment-thickness-adapted grid, where the thickness of sediment layers varies with time to accommodate the deposited sediment. Horizontal resolution within sediments follows the resolution of the water column grid.

The biogeochemical model is organised into 3 zones: pelagic, epibenthic and sediment. The epibenthic zone overlaps with the lowest pelagic layer and the top sediment layer, sharing the same dissolved and suspended particulate material fields. Dissolved and particulate biogeochemical tracers are advected and diffused throughout the model domain. Additionally, biogeochemical particulate substances sink and are resuspended in the same way as sediment particles. Biogeochemical processes are organized into pelagic processes of phytoplankton and zooplankton growth and mortality, remineralisation of particulate and organic material, and fluxes of dissolved oxygen, nitrogen, phosphorus and carbon (including nitrogen fixation, phosphorus adsorption and desorption, surface gas exchanges, respiration and phorosythensis, and fluxes to and from biotic pools); epibenthic processes of growth and mortality of macroalgae, seagrass and corals, and sediment based processes of phytoplankton mortality, microphytobenthos growth, detrital remineralisation and fluxes of dissolved substances (Fig.2).

The biogeochemical model includes four groups of microalgae (small and large phytoplankton, *Trichodesmium* and microphytobenthos) and three macrophytes types (seagrass types corresponding to *Zostera* and *Halophila*, macroalgae and coral communities). Photosynthetic growth is determined by concentrations of dissolved nutrients (nitrogen and phosphate) and photosynthetically active radiation. Autotrophs take up dissolved ammonium, nitrate, phosphate and inorganic carbon, and in the case of

Trichodesmium, fix atmospheric nitrogen (Robson et al., 2014). Microalgae incorporate carbon (C), nitrogen (N) and phosphorus (P) at the Redfield ratio (106C:16N:1P, Redfield 1963) while macrophytes do so at the Atkinson ratio (550C:30N:1P, Atkinson1983). Microalgae contain two pigments (chlorophyll-*a* and an accessory pigment), and have variable carbon:pigment ratios determined using a photoadaptation model (described in Baird et al., 2013).

Micro-zooplankton graze on small phytoplankton and meso-zooplankton graze on large phytoplankton and microzooplankton, at rates determined by particle encounter rates and maximum ingestion rates. Of the grazed material that is not incorporated into zooplankton biomass, half is released as dissolved and particulate carbon, nitrogen and phosphate, with the remainder forming detritus. Additional detritus accumulates by mortality. Detritus and dissolved organic substances are remineralised into inorganic carbon, nitrogen and phosphate with labile detritus transformed most rapidly (days), refractory detritus slower (months) and dissolved organic material transformed over the longest timescales (years). The production (by photosynthesis) and consumption (by respiration and remineralisation) of dissolved oxygen is also included in the model and depending on prevailing concentrations, facilitates or inhibits the oxidation of ammonia to nitrate and its subsequent denitrification (in the sediment) to di-nitrogen gas which is then lost from the system. Full details of equations used in the biogeochemical model are given by Baird et al. (2016b) and details of parameter values and implementation for the Great Barrier Reef are given by Herzfeld et al. 2016

The model is forced using flow and concentrations of dissolved and particulate constituents from 21 rivers along the Queensland coast (north to south: Normanby, Daintree, Barron, combined Mulgrave+Russell, Johnstone, Tully, Herbert, Haughton, Burdekin, Don, O'Connell, Pioneer, Fitzroy, Burnett, Mary, Calliope, Boyne, Caboolture, Pine, combined Brisbane+Bremer, and combined Logan+Albert) and the Fly River in Papua New Guinea (Herzfeld et al., 2015). To determine river concentrations, sediment and nutrient observations were statistically evaluated over 10 years (Furnas 2003). Separate analysis was undertaken for wet- (the Fly, and the northern most 6 rivers in Queensland) and dry- (remainder) catchment rivers. Volume-averaged wet season export coefficients based on this observed dataset were derived for wet- and dry-catchment river types, and mean flow-weighted concentrations determined. These constant concentrations are multiplied by higher frequency (daily) observed discharge data to calculate the flux of constituents at the river mouths.

The eReefs BGC and sediment model has 3 open ocean boundaries. Nutrient concentrations flowing in from the boundaries were obtained from the CSIRO Atlas of Regional Seas (CARS) 2009 climatology (Ridgway et al., 2003) and empirical nutrient-temperature relationships. The initial conditions are specified by a generalised empirical relationship and scaled nutrient profiles on the model density profile specifying top and bottom water column values from CARS ocean atlas. Surface NO_3 is usually low (< 3 mg m^{-3}). In deeper waters nutrient concentrations increase from 0 to 1500 m depth and then remain constant down to the ocean floor (4000 m depth, 500 mg m^{-3}). The initial conditions for most other tracers were not spatially resolved, since observations for the outer reef and Coral Sea are limited temporally and spatially.

Tables:

Table 1: The subset of state variables included in the state vector and corresponding observation error standard deviations used for four assimilation system configurations. The bold variables in the state vector are used in the input to the observation operator. It should be noted than the state variables are transformed by taking the natural logarithm of the variables. The observation error is then applied to the log-transformed state vector.

	Assimilation State Vector (**X**)	Observation Error (**R**)
EXP1	Log(**Surface Total Chl-a**, PhyS Chl-a, PhyL Chl-a)	0.8
EXP2	Log(**Simulated OC3M**, PhyS Chl-a, PhyL Chl-a)	0.8
EXP3	Log(**Simulated OC3M**, PhyS Chl-a, PhyL Chl-a)	0.4
EXP4	Log(**Simulated OC3M**, PhyS Chl-a, PhyL Chl-a, NO3, NH4, TSS)	0.4

Table 2: Forecast error statistics for EXP4 by region (inshore, lagoon, offshore) for the Control (C), Forecast (F), Analysis (A) and Persistence (P) fields.

Region	Whole of Domain				Coastal				Lagoon and Shelf				Oceanic			
Field	C	F	A	P	C	F	A	P	C	F	A	P	C	F	A	P
Median	0.32	0.23	0.19	0.26	1.35	1.29	1.12	1.46	0.34	0.25	0.19	0.25	0.16	0.1	0.06	0.11
Mean	0.37	0.24	0.2	0.27	1.92	1.37	1.25	1.46	0.38	0.24	0.2	0.25	0.16	0.1	0.06	0.11
25% Quartile	0.27	0.2	0.14	0.21	1.1	0.95	0.92	0.94	0.29	0.16	0.14	0.21	0.14	0.08	0.04	0.7
75% Quartile	0.48	0.3	0.23	0.29	2.45	1.87	1.64	1.08	0.43	0.29	0.22	0.29	0.19	0.13	0.08	0.12

Table 3: Forecast Percentage errors for EXP4 by region (inshore, lagoon, offshore) for the Control (C), Forecast (F), Analysis (A) and Persistence (P) fields.

Region	Whole of Domain				Coastal				Lagoon and Shelf				Oceanic			
Field	C	F	A	P	C	F	A	P	C	F	A	P	C	F	A	P
Median	100	53	39	53	130	95	90	105	95	47	38	52	93	48	31	48
Mean	107	54	38	55	180	97	90	107	102	51	37	56	96	50	31	51
25% Quartile	81	41	35	42	105	105	95	74	75	43	36	41	71	44	35	39
75% Quartile	131	61	41	62	181	85	81	145	118	62	42	62	126	55	30	62
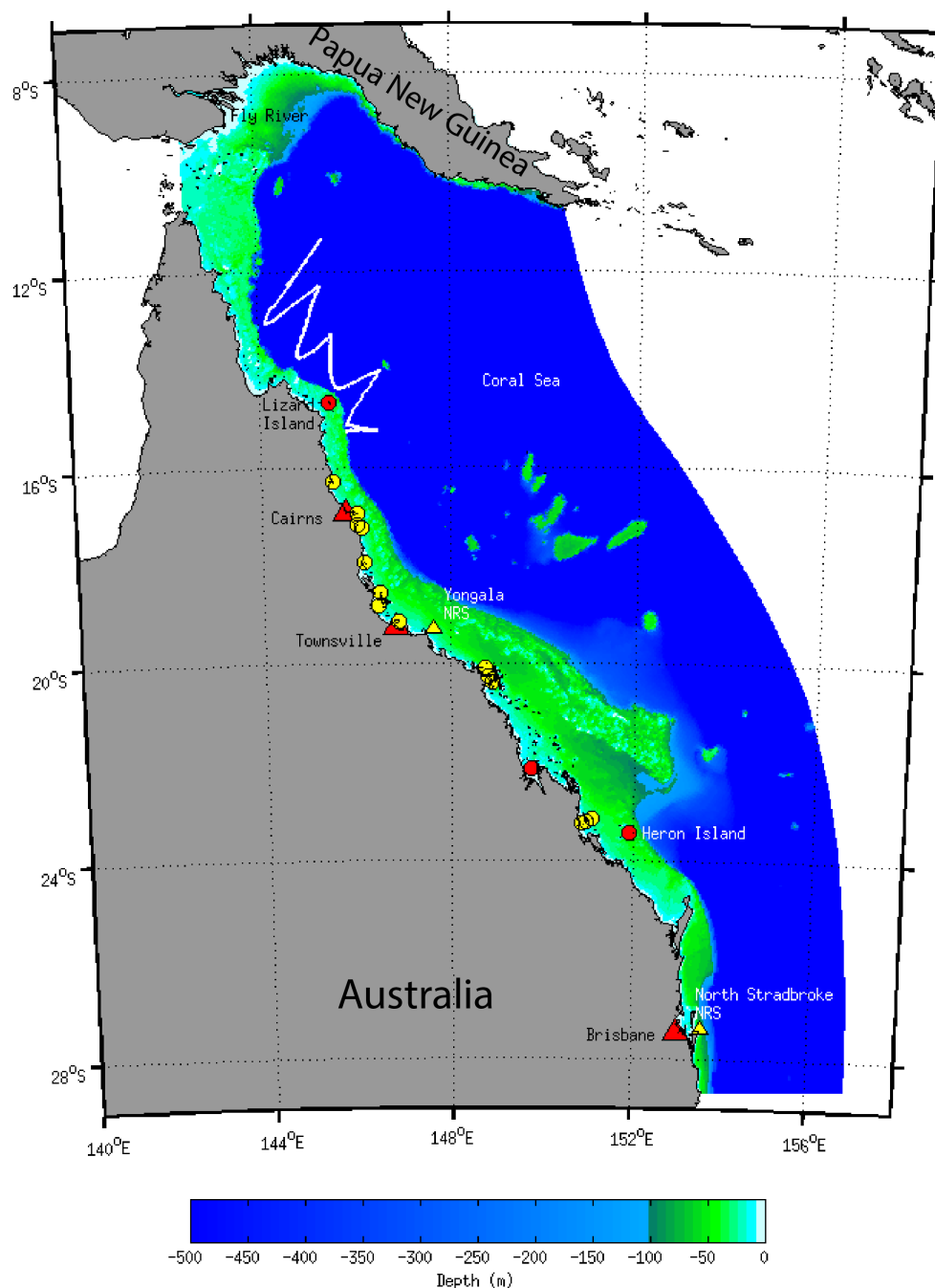
Figures:

Figure 1: A map of the Great Barrier Reef region, with the color bar denoting the water depth, markers denote the population centres (red triangles), IMOS NRS sites (yellow triangles), Reef Rescue WQMs (yellow circles) and points of interest referred to in the text (red circles), with the glider track (white line adjacent to Lizard Island). The *in-situ* sampling locations and glider observations are used to assess the data assimilation system performance, using the EXP4 configuration.
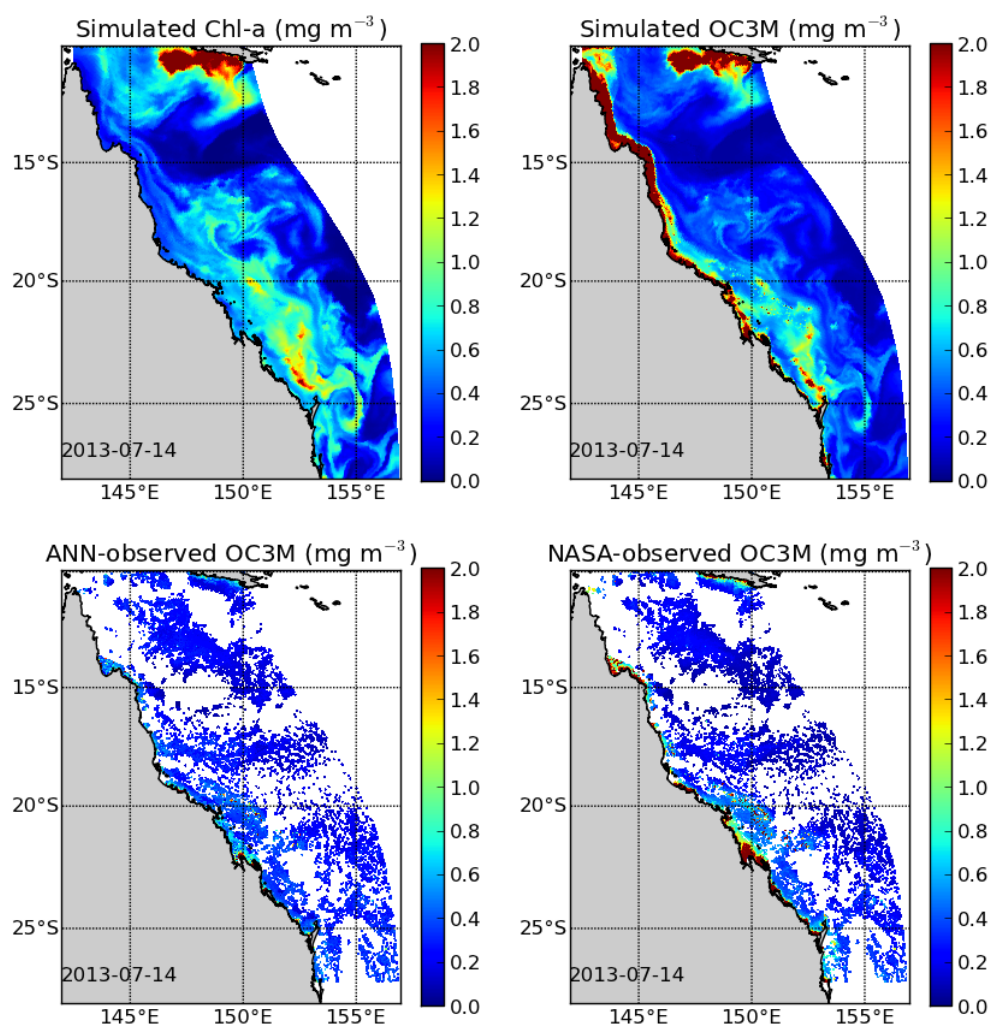
Figure 2: Simulated surface Chl-a (mg m⁻³) of the non-assimilating control run (top left) and the simulated OC3M (top right) derived from the simulated remote-sensing reflectance for the 14/7/2013. The observed OC3M with ANN-derived observed remote-sensing reflectance (bottom left) and NASA-derived observed remote-sensing reflectance (bottom right).
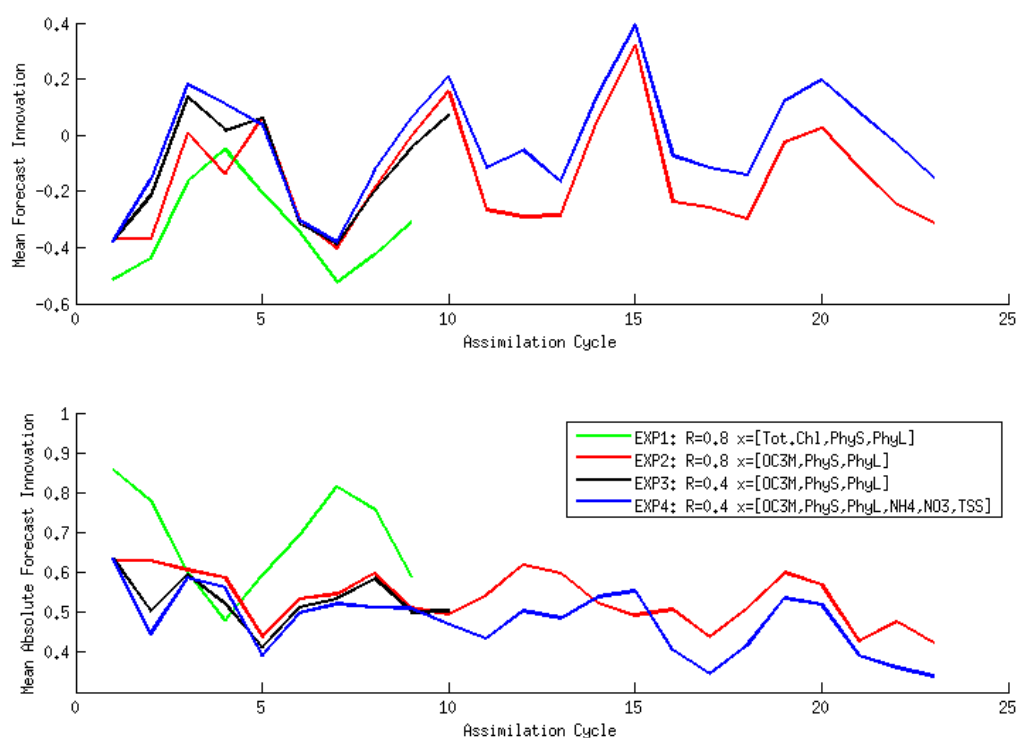
Figure 3: Comparison of innovation statistics for the four assimilation experiments undertaken, where 0 indicates perfect agreement between model and observations. The top panel plots the mean innovation for each assimilation cycle. The lower panel plots the mean absolute innovation against assimilation cycle. The following colours correspond to: green (EXP1), red (EXP2), black (EXP3) and blue (EXP4). The variables in the legend correspond to the observation error (R) and the assimilation state vector (X).
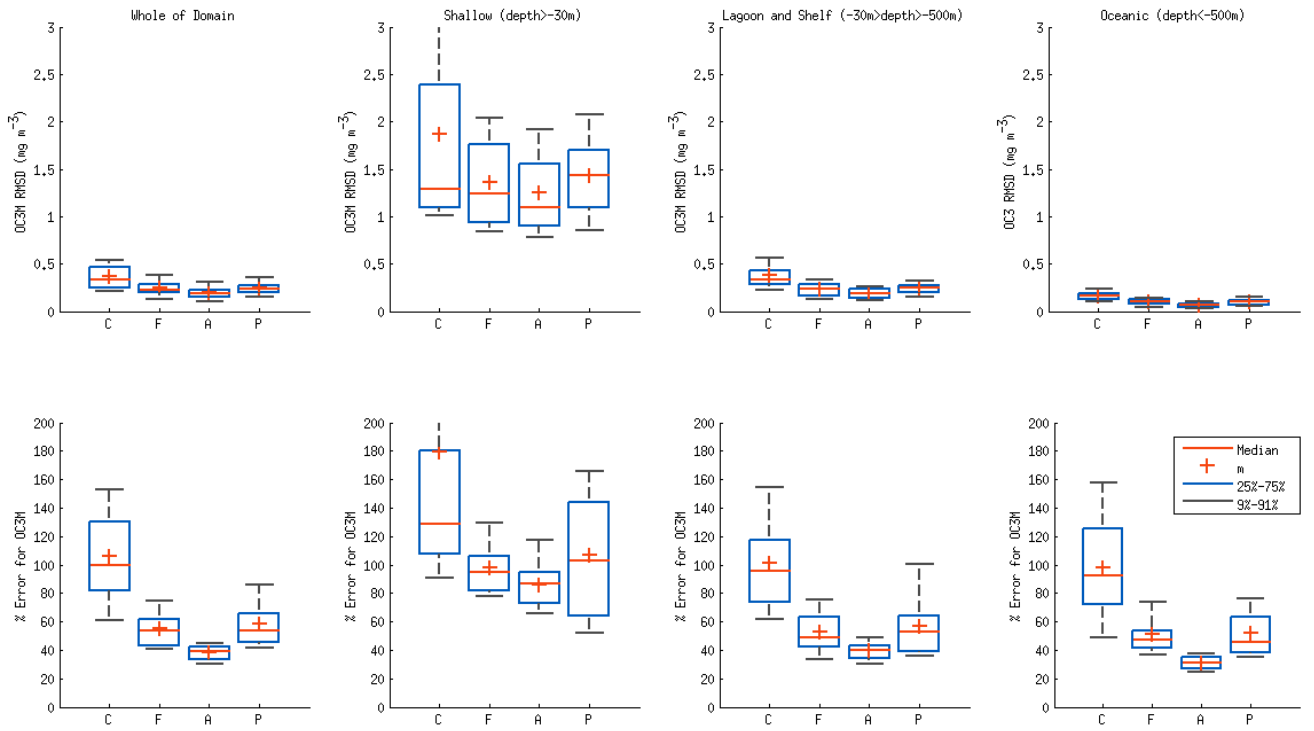
Figure 4: Box and whisker plots of RMSD (top row) and MAPE (bottom row) of the mis-match between simulated OC3M and ANN-observed OC3M. Each panel contains the control run (C) and EXP4 showing forecast (F), persistence (P) and analysis (A). Presented are statistics for the whole domain (left column), and for specific depth ranges (three rightmost columns).
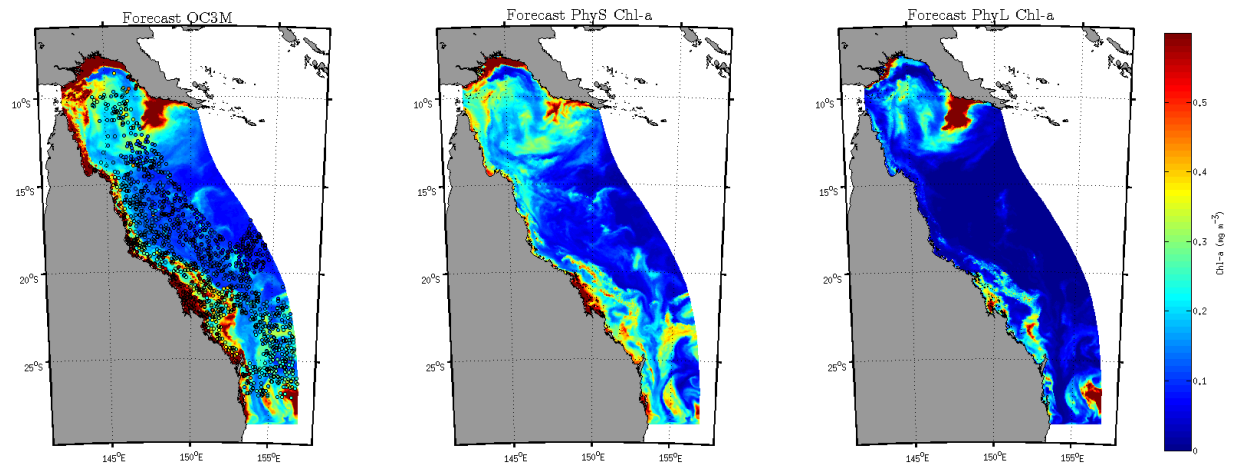
Figure 5: Simulated (forecast) OC3M (left) for cycle 22 (12th September 2013) with observations overlaid, surface Small Phytoplankton (PhyS) Chl-a (centre) and surface Large Phytoplankton (PhyL) Chl-a (right).
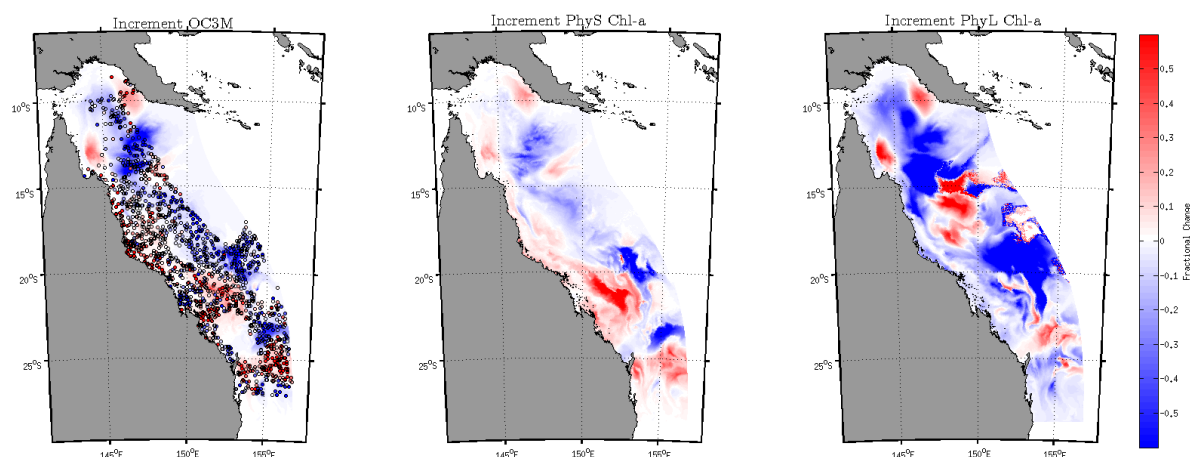
Figure 6: Increments that are added to the forecast fields generated by the assimilation system for simulated OC3M with innovations overlaid (left), and the prognostic variables of surface small phytoplankton Chl-a (centre) and surface large phytoplankton Chl-a (right).
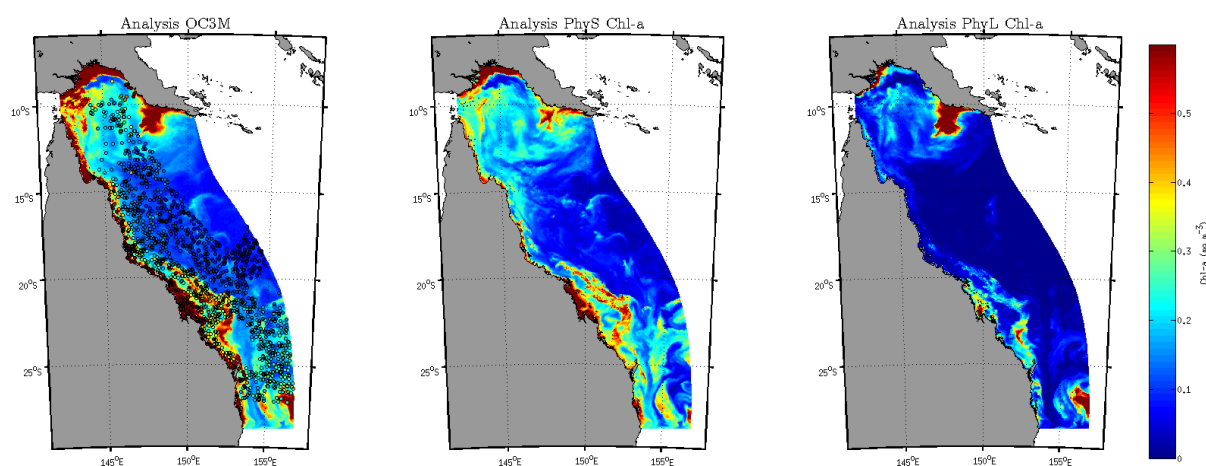
Figure 7: The resulting analysis fields for simulated OC3M and withheld ANN OC3M observations overlaid (left), and the analysis fields for the prognostic variables of small phytoplankton (centre) and large phytoplankton (right) for the 12th September, 2013.
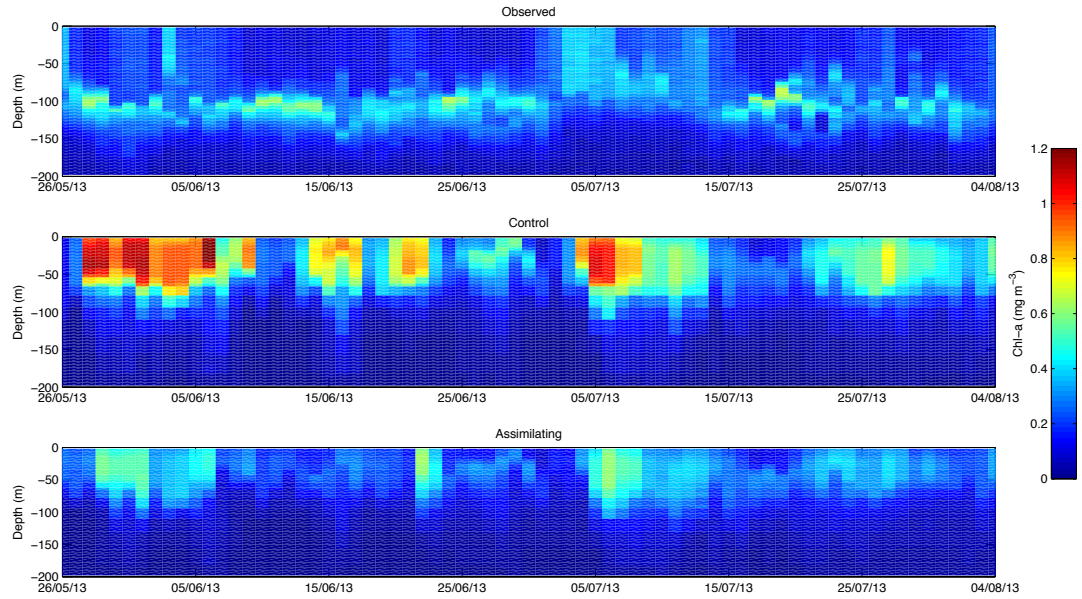
Figure 8: Comparison against independent IMOS glider observations, with the observed section of Chl-a derived from the onboard fluorescence sensor. The comparison is undertaken in model space, whereby all glider data that fall within a 1 hour window either side of when there is a 3D model output available is extracted, and equivalent simulated Chl-a are extracted from the model. The glider and model data is then spatially aggregated and interpolated onto the vertical model grid. The resulting section for the glider (top), and the simulated glider sections from the non-assimilating model (centre) and assimilating model (bottom).
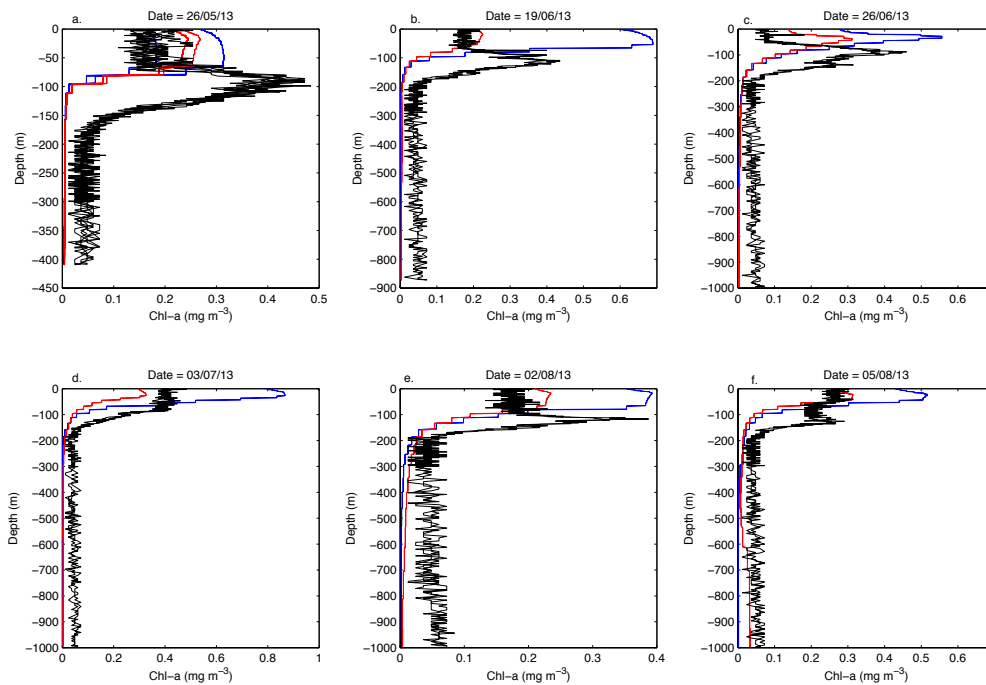
Figure 9: Comparison of depth-resolved Chl-a against six individual glider profiles using the method described in the caption of Figure 8. Glider observations are black, the non-assimilating control run profiles are blue, and the assimilating run profiles are red.
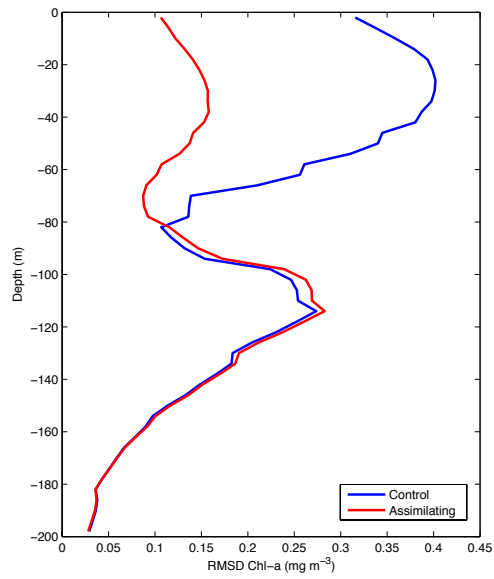
Figure 10: A profile of the temporal mean Chl-a RMSD between the glider observations presented in Figure 8 and the non-assimilating (blue) and assimilating (red) runs.
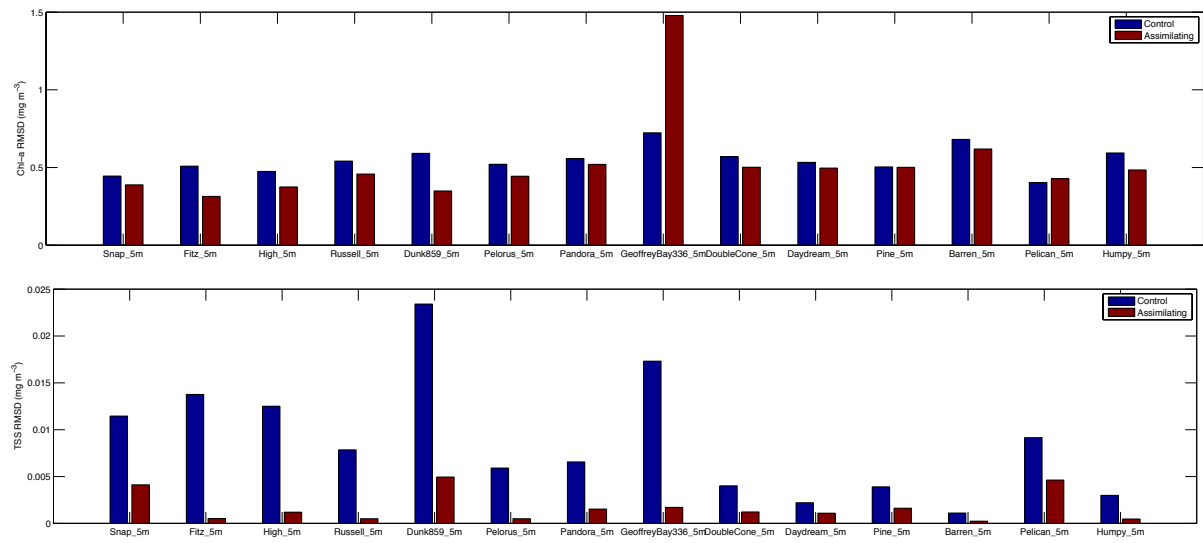
5   **Figure 11: A comparison of Chl-a and TSS RMSDs between the in-situ AIMS Reef Rescue moorings for the non-assimilating (blue) and assimilating (red) model runs, the Reef Rescue sites are denoted by the yellow circles in Figure 1.**
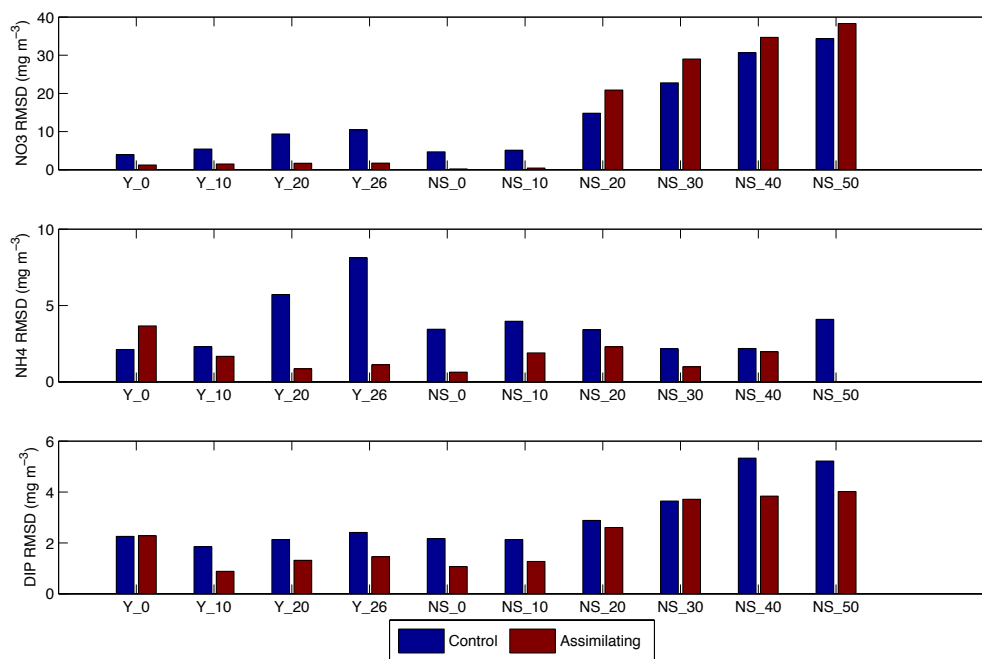
Figure 12: A comparison of RMSD of simulated nutrients with in-situ bottle samples for the non-assimilating (blue) and assimilating (red) model runs. Observations are obtained at the Queensland IMOS site (yellow triangles in Figure 1) at Yongala (Y) and North Stradbroke (NS) Island. Y_0 are the Yongala surface samples, while Y_26 are the samples taken from 26 m depth.
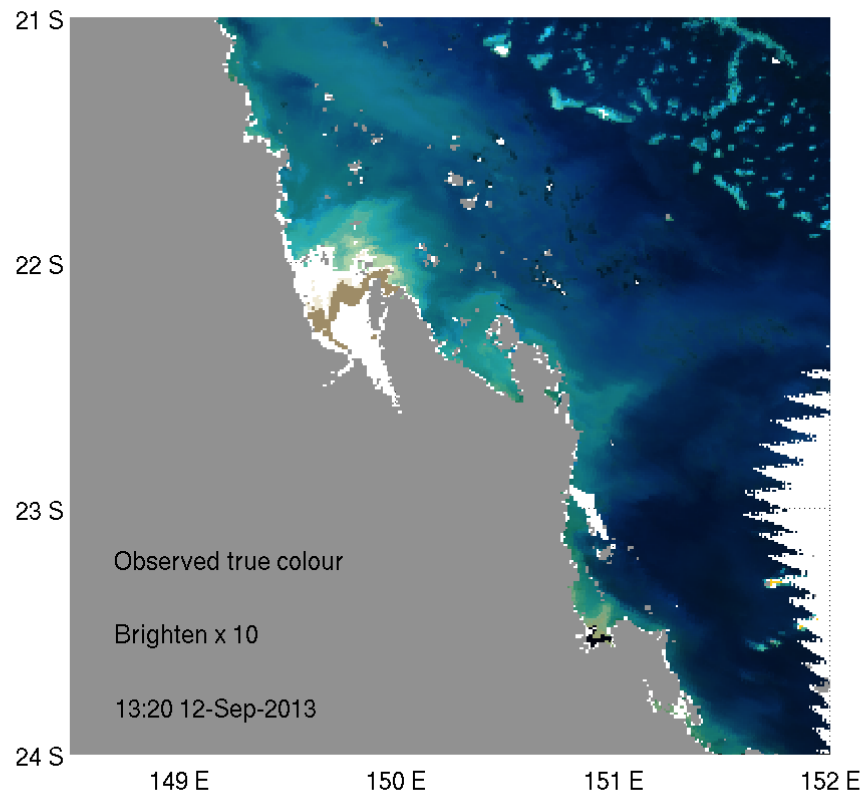
Figure 13: Observed true-colour image on the 12 Sep 2013 obtained from 1 km resolution, atmospherically-corrected ANN remote-sensing reflectance. The RGB wavelengths used were 667, 551 and 488 nm and processed using the MODIS

true colour algorithm (Gumley et et al., 2010; Baird et al., 2016). The white pixels are clouds, grey is land. Simulated true colour images are not falsely-coloured, thus do not require a colour map, nor are they 2D as they have a depth of field, being based on reflectance from multiple depths and the bottom (Baird et al., 2016a). Thus simulated true colour can be considered a photograph of the optical state of the different model runs, and, like observed true colour, a powerful and intuitive visualisation tool for water clarity in biogeochemical models.
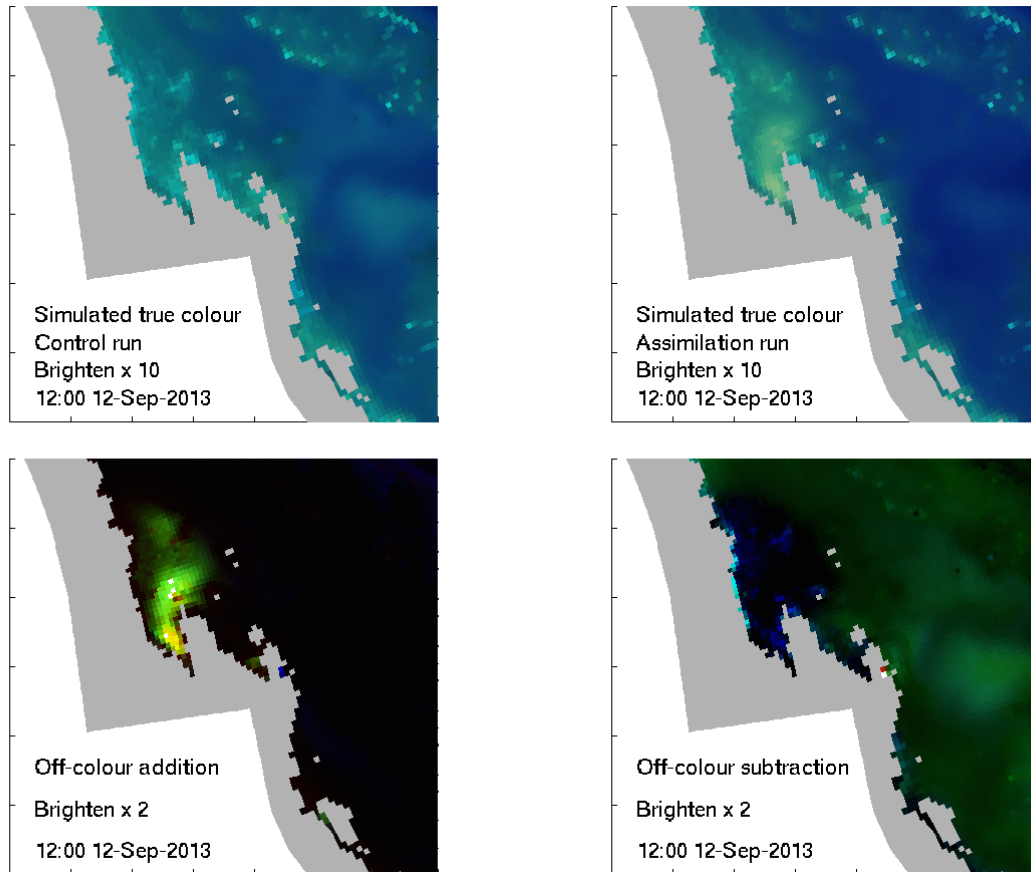
Figure 14: The simulated true-colour image on the 12 Sep 2013 of the control run (top left) and assimilation run (top right). The difference between the remote-sensing reflectance in the control and assimilated runs was used to quantify the colour (referred to as off-colour) added (i.e. greater surface expression, bottom left) and subtracted (i.e. less surface expression, bottom right) due to the updating of optically-active constituents in the assimilation run (see Fig. 13 for more details). Note that the off-colour images have a smaller brightening factor as the MODIS true colour stretch saturates the features that are of most interest.
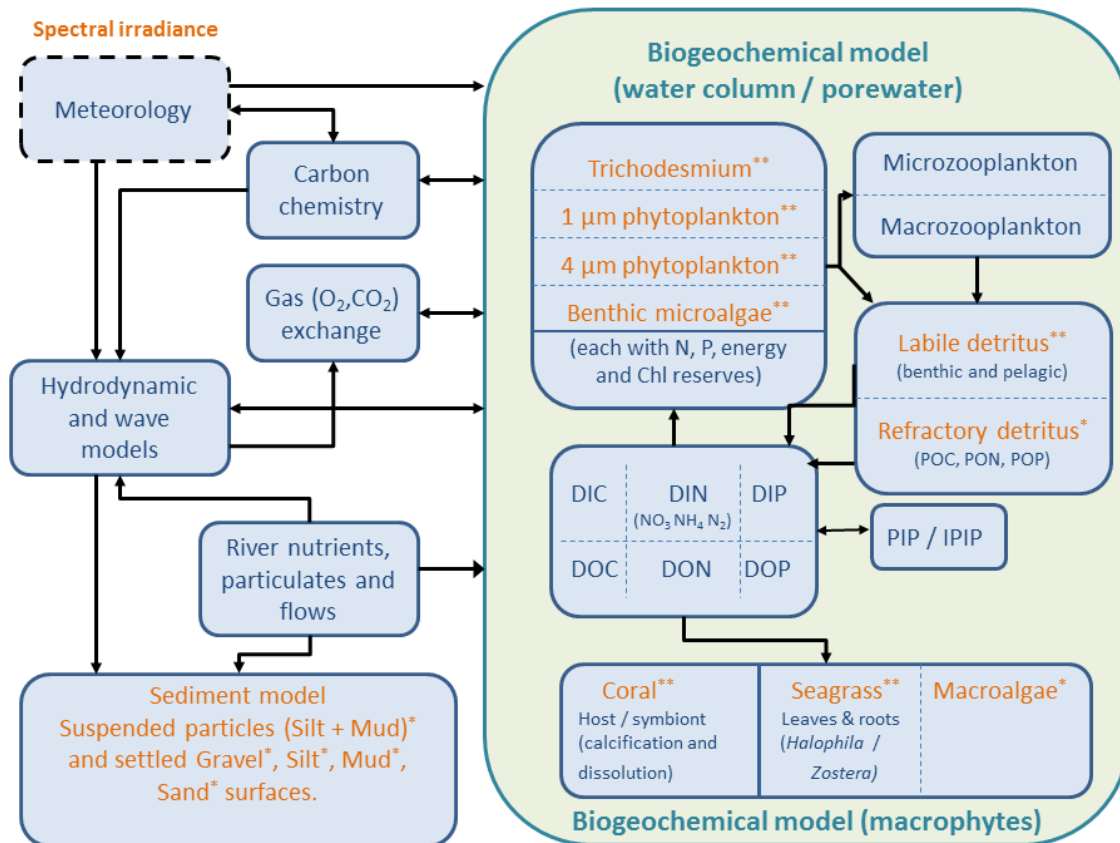
Figure 15: The eReefs modelling system with optically-active components identified with beige colouring and an asterisk, with the number of asterisks denoting the number of different optically-active elements with this component. Thus, each of the four microalgae microalgae have two pigment types, one absorbing like divinyl chlorophyll-a, and the other like photosynthetic carotenoids; there are two seagrass types, corals have both skeletons and zooxanthellae; three types of detritus absorb and scatter, and the sediment model contains a suspended fraction and four (mixed) sediment compositions. Additionally, pure seawater both absorbs and scatters light.